Dissertation

Submitted to the

Combined Faculty of Natural Sciences and Mathematics

of Heidelberg University, Germany

for the degree of

Doctor of Natural Sciences

Put forward by

Thomas Cameron Harris

born in: Lake Forest, Illinois, USA

Oral examination: November 10, 2021

A Novel Megavoltage Multilayer Imager Improves Clinical Beam's-Eye-View Performance

Referees: Prof. Dr. Joao Seco

                       Prof. Dr. Jürgen Hesser

Abstract

Megavoltage imaging offers unique clinical applications due to providing a beam's-eye-view of the actual radiation delivery. However, poor electronic portal imaging device (EPID) performance presently limits the clinical utility of megavoltage imaging. This thesis describes the clinical translation, implementation, and trial of a novel multilayer imager (MLI) designed to address current EPID shortcomings, as well as the development of an application using the imager to track tumor location during treatment.

The prototype MLI was constructed, with standard imaging metrics demonstrating a 5.7x increase in detective quantum efficiency, as well as substantially improved contrast- and signal-to-noise ratios compared to standard EPID. Pre-clinical tests were performed on an anthropomorphic phantom to verify improved performance despite anatomical variations. Subsequently, we conducted a clinical trial of six patients receiving radiation for liver metastases. A beam's-eye-view tumor tracking algorithm was utilized to assess MLI performance compared to a standard single layer imager. Tumor tracking using MLI was found to be significantly more accurate and efficient at successfully tracking on more frames. Further analysis revealed correlation between noise reduction and improved tracking performance. Given the MLI's superior performance, for clinical beam's-eye applications we recommend noise reduction strategies such as employing multiple detection layers in the EPID.

Zusammenfassung

Die Megavolt (MV)-Bildgebung bietet einzigartige klinische Anwendungen, da sie Bilder aus der Sicht des Strahls, die so gennante Beams-Eye-View (BEV), liefert. Jedoch begrenzt die derzeit Qualität der Bilder der elektronischen Portal-Bildgebungsvorrichtung (EPID) die klinischen Nutzung. Diese Dissertation beschreibt die klinische Umsetzung, Implementierung und Erprobung eines neuartigen Multilayer-Imagers (MLI), der die aktuellen EPID-Mängel beheben soll, sowie die Entwicklung einer Anwendung, die es ermöglicht den Tumor während der Behandlung zu verfolgen.

Der genutzte Prototyp des MLI wurde konstruiert und erste Tests zeigen eine im Vergleich zum Standard-EPID eine 5,7-fache Steigerung der detektiven Quanteneffizienz sowie ein wesentlich verbessertes Kontrast-Rausch-Verhältnis. Um eine verbesserte Leistung trotz anatomischer Variationen zu überprüfen Vorklinische Tests wurden an einem anthropomorphen Phantom durchgeführt. Anschließend führten wir eine klinische Studie mit sechs Patienten mit Lebermetastasen durch. Ein Tumorverfolgungsalgorithmus basierend auf der BEV wurde verwendet, um das MLI-basierende Tracking im Vergleich zu einem konventionellem System zu charakterisieren. Es wurde festgestellt, dass die Tumorverfolgung mit dem MLI Prototypen signifikant genauer und effizienter ist. Eine weitere Analyse ergab eine Korrelation zwischen der Rauschunterdrückung und einer gesteigerte Genauigkeit der Tumorverfolgung. Angesichts der überragenden Leistung des MLI empfehlen wir für klinische BEV-Anwendungen Strategien zur Rauschunterdrückung wie die Verwendung mehrerer Detektionsschichten im EPID.

Contents

v

List of figures

List of Abbreviations

BEV	Beam's-eye-view
CBCT	Conebeam CT
CNR	Contrast-to-noise ratio
CT	Computer tomography
DPE	Detective quantum efficiency
EPID	Electronic portal imaging device
MLI	Multilayer imager
MTF	Modulation transfer function
nNPS	Normalized noise power spectrum
NPS	Noise power spectrum
RMSE	Root mean square error
SBRT	Stereotactic body radiation therapy
SNR	Signal-to-noise ratio
TFT	Thin film transistor
VMAT	Volumetric modulated arc therapy

Chapter 1

Introduction

1.1 Motivation

Many oncology patients receive external beam radiation as either a stand-alone therapy or in combination with other modalities such as surgery and chemotherapy. "On-board imaging" integrated into the linear accelerator has advanced over the years, allowing better localization of the target at each dose delivery. Better localization allows reduction of the extra margin added to the target meant to ensure the tumor is not missed. This confers dosimetric and clinical benefits, including potential reduction of radiation side effects (Kitamura et al. 2003). Common side effects vary by treatment site, but examples include pneumonitis, fecal and urinary incontinence, lymphedema, nausea, and secondary malignancies. Monitoring of tumor motion during dose delivery is also possible (Shimizu et al. 2001), allowing motion management strategies such as gating or tumor tracking.

Electronic on-board imaging was initially implemented by placing an imaging panel (electronic imaging portal device, or EPID) in the path of the radiation beam but on the other side of the patient, collecting radiation that has passed through the body (Herman *et al.* 2001). The resulting images can be used to ensure that the radiation beam is aligned with the expected location of the target. Because the treatment radiation beam is of megavoltage energy -- unlike diagnostic radiation, which is in the kilovoltage range -- the radiation is so penetrating that tissue contrast is poor and most radiation (~99% of incident photons) passes through the detector without interaction (Antonuk 2002). Later, kilovoltage sources and detectors were installed on linear accelerators orthogonal to the treatment beam (Jaffray *et al.* 2002) as shown in Figure 1. These sources operate at energies similar to conventional CT scanners and provide improved tissue contrast and higher detective efficiency (Kriminski *et al.* 2008). In order to take planar images similar to radiographs, the kV system

can be operated while the gantry rotates to create a 3-D reconstruction of the target area through a process called conebeam CT (CBCT) (Jaffray *et al.* 2002). These planar images and CBCTs can be used prior to treatment to verify that the target will be aligned with the radiation beam. Additionally, kV images can be taken during beam delivery to assess if the tumor has moved during the actual treatment (Soete *et al.* 2007).
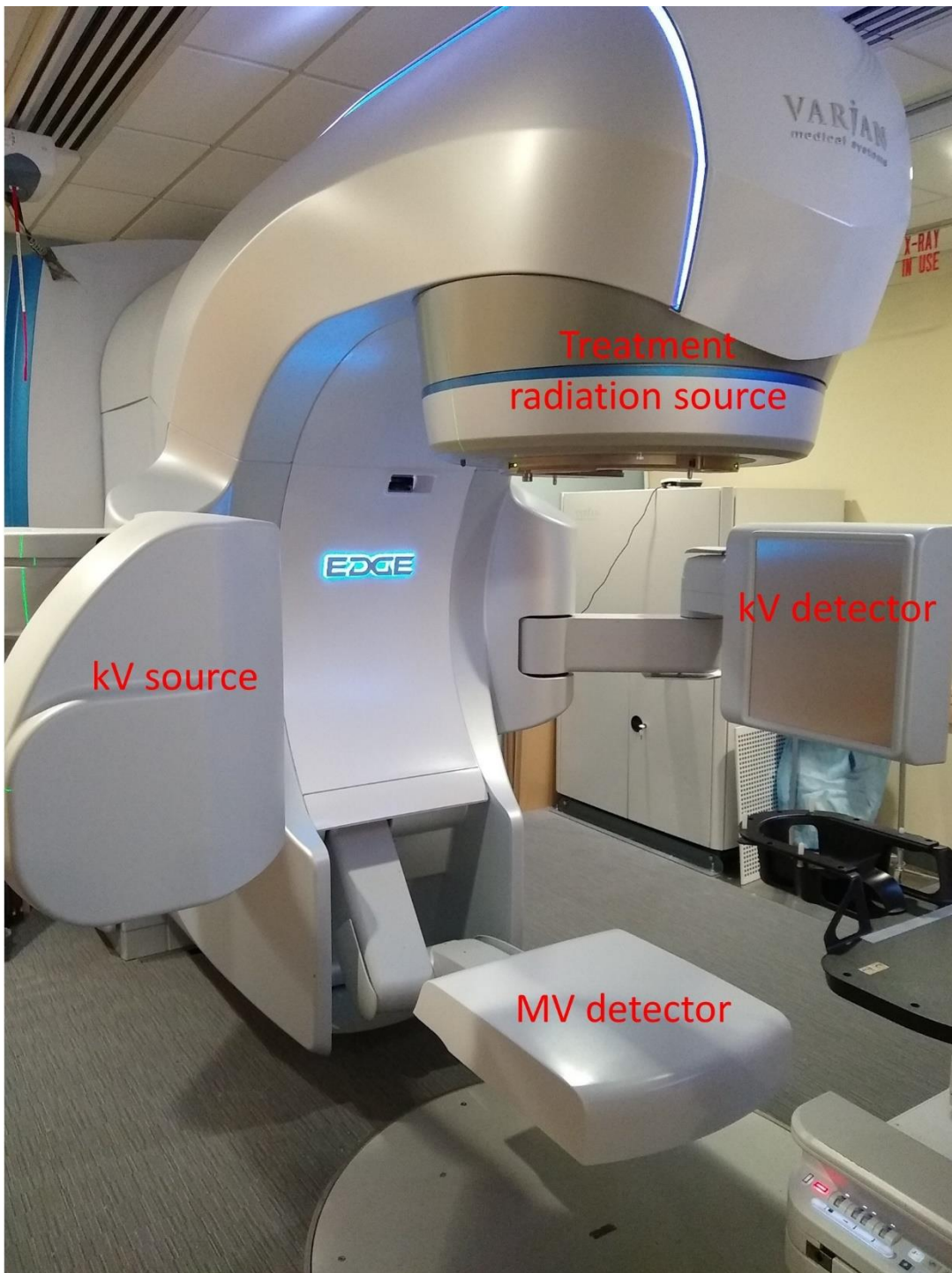
Figure 1: the linear accelerator used in the thesis experiments with the treatment radiation source and imaging components labeled.

While exclusively using kV imaging may seem appealing due to the better image quality it affords, MV imaging offers unique advantages that can be exploited.   EPIDs image the exact tissues and structures irradiated by the

treatment beam, providing a so-called beam's-eye-view (BEV) rather than an orthogonal view.   This is particularly important for clinical applications such as tumor tracking during treatment.   As shown in Figure 2, after the initial build-up region (through 1.5cm), the percent depth dose curve for a typical treatment beam will not vary significantly with small changes in depth, but can lead to significant tumor underdoses if misaligned in the BEV frame.   Orthogonal kV beams are degenerate in one of the two BEV dimensions.   A further advantage to MV imaging is that the EPID can use information from the treatment beam itself, generating images without giving additional radiation dose to the patient (as is the case in kV imaging).
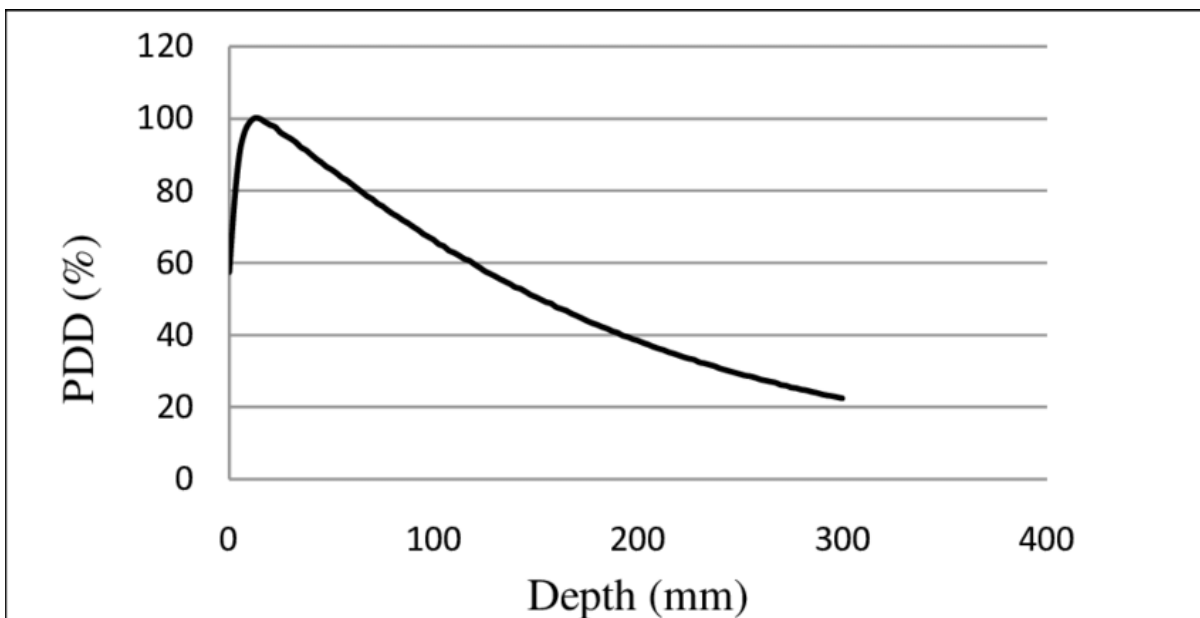
Figure 2: The percent dose of a 6 MV beam deposited as a function of depth, normalized to the maximum dose.

As noted previously, current EPIDs are limited by poor tissue contrast and detection efficiency, which causes significant difficulty in exploiting the native advantages of MV imaging. Improving the design of EPIDs could improve treatment efficacy and reduce side effects in cancer patients receiving radiation. This thesis addresses the development and testing of a novel EPID.

1.2 Aim of this thesis

This thesis presents the results of a multi-stage project focused on developing and implementing a new multilayer design for EPIDs.   Our novel EPID, a "Multilayer Imager" (MLI), is comprised of four vertically stacked imaging layers. The initial goal was to demonstrate that the new model has improved imaging metrics, and that the multilayer approach may improve future imager designs. Subsequently, we quantified the extent to which the better performance translates into better results of clinical applications when used to image live patients.

The first step towards this goal was creating software using Matlab that would allow an EPID to track tumor position using the radiation treatment beam during complex treatment plan delivery.   The code would read in the acquired images and return the position of the tumor.   The resulting algorithm benefits the radiation oncology field as a stand-alone application to monitor tumor motion, while also utilizable by our group for testing the capabilities of the prototype EPID.   The details of this work are presented in the manuscript replicated in chapter 2.1.

Before deploying the prototype, we measured its performance on standard imaging metrics.   Its performance on anthropomorphic phantoms was also evaluated as part of the process of translating the device to clinical use.   The MLI's performance was compared to the results of a standard single layer EPID. The findings of this work can be found in the manuscript replicated in chapter 2.2.

Finally, the prototype was tested in actual clinical situations.   Approved by the Dana-Farber Cancer Institute's institutional review board, a clinical trial of patients receiving radiotherapy for liver metastases was conducted.   Data for each patient was gathered both using the MLI and with a single layer imager to allow comparison.   The algorithm from chapter 2.1 with some modifications was used to conduct the comparison.   This experiment was important to show that the MLI not only has improved imaging metrics, but that the improvements are measurable when imaging live patients with their complex and irregular

geometries. This manuscript describing this experiment is presented in chapter 2.3.

Chapter 2

Publications

This thesis is presented in cumulative format according to the regulations of the Department of Physics and Astronomy of Heidelberg University. All of the manuscripts have been published in internationally acclaimed peer reviewed journals. A statement describing the thesis author's contributions to the publication precedes each article.

2.1 Automated MV markerless tumor tracking for VMAT

This manuscript describes the generation of a markerless tumor tracking algorithm using data collected by an EPID during radiation treatments involving complex gantry and aperture motion.   It opens with a detailed explication of the theory governing functioning of the algorithm, and subsequently describes the results of tests run on a dynamic motion thorax phantom programmed with known tumor translation and rotation parameters to mimic a patient's respiration.   The algorithm was also tested on preliminary patient data being gathered for the research that ultimately resulted in the manuscript reproduced in chapter 2.3.

The thesis author contributed to the design and coding of the algorithm.   In addition, he helped design and gather data for the dynamic phantom experiment.   He also acquired the patient data for the final test.   He contributed to data analysis, as well as to preparation of the final manuscript.

The thesis author is a medical physicist certified by the American Board of Radiology with fifteen years of clinical experience as a physicist in varied practice settings (both tertiary care academic and community hospitals), as well as three previous years of clinical experience as a medical dosimetrist. He has worked in a variety of clinical capacities encompassing multiple disease types (both oncology and non-oncology applications) and including both external beam radiotherapy and brachytherapy. His familiarity with the field of radiation oncology was essential for assisting the first author in developing clinically relevant endpoints for the software.   His contributions also heavily leveraged an extensive knowledge of the capability and operations of the relevant radiation oncology hardware and software needed to gather and process data.

After publication of this manuscript, the thesis author took over full responsibility for the maintenance of the algorithm, allowing its future use by the research group. He also continued to grow the code's functionality, allowing it to focus solely on implanted markers when necessary, instead of solely seeking any region of high

variance for tracking. This additional functionality would prove essential to future research on the MLI's capabilities, particularly for the head-to-head comparison with a single layer imager in the chapter 2.3 manuscript.

Physics in Medicine & Biology

IPEM Institute of Physics and Engineering in Medicine

PAPER

Automated MV markerless tumor tracking for VMAT

D Ferguson[1], T Harris[1], M Shi[1,4], M Jacobson[1], M Myronakis[1], M Lehmann[2], P Huber[2], D Morf[2],
R Fueglistaller[2], P Baturin[3], I Valencia Lozano[1], C Williams[1] and R Berbeco[1]

[1] Brigham and Women's Hospital, Dana-Farber Cancer Institute, and Harvard Medical School, Boston, MA, United States of America
[2] Varian Medical Systems, Baden-Dattwil, Switzerland
[3] Varian Medical Systems, Palo Alto, CA, United States of America
[4] University of Massachusetts, Lowell, Lowell, MA, United States of America

E-mail: dianne_ferguson@dfci.harvard.edu

Abstract

Tumor tracking during radiotherapy treatment can improve dose accuracy, conformity and sparing of healthy tissue. Many methods have been introduced to tackle this challenge utilizing multiple imaging modalities, including a template matching based approach using the megavoltage (MV) on-board portal imager demonstrated on 3D conformal treatments. However, the complexity of treatments is evolving with the introduction of VMAT and IMRT, and successful motion management is becoming more important due to a trend towards hypofractionation.

We have developed a markerless lung tumor tracking algorithm, utilizing the electronic portal imager (EPID) of the treatment machine. The algorithm has been specifically adapted to track during complex treatment deliveries with gantry and MLC motion. The core of the algorithm is an adaptive template matching method that relies on template stability metrics and local relative orientations to perform multiple feature tracking simultaneously. Only a single image is required to initialize the algorithm and features are automatically added, modified or removed in response to the input images. This algorithm was evaluated against images collected during VMAT arcs of a dynamic thorax phantom. Dynamic phantom images were collected during radiation delivery for multiple lung SBRT breathing traces and an example patient data set. The tracking error was 1.34 mm for the phantom data and 0.68 mm for the patient data.

A multi-region, markerless tracking algorithm has been developed, capable of tracking multiple features simultaneously without requiring any other *a priori* information. This novel approach delivers robust target localization during complex treatment delivery. The reported tracking error is similar to previous reports for 3D conformal treatments.

1. Introduction

Addressing tumor motion during radiotherapy treatment is integral to ensuring the target receives the prescribed dose. The amplitude of motion is dependent on anatomical location, and can be relatively large for lung cases (up to 2 cm) (Ekberg *et al* 1998, Seppenwoolde *et al* 2002, Keall *et al* 2006), and also for prostate (Kitamura *et al* 2002), adrenal (Katoh *et al* 2008) and liver (Liang *et al* 2018). With the introduction of intensity-modulated radiation therapy (IMRT), highly conformal treatments with steep dose fall-offs can be delivered more easily. However, the limit to faithfully delivering the planned treatment dose while reducing dose to healthy tissue is still constrained by the gross tumor volume (GTV) expansions for tumor motion. The emergence of advanced modalities like hypofractionated stereotactic body radiation therapy (SBRT) and adaptive radiotherapy provides further impetus for robust motion management.

A variety of strategies have been developed to address tumor motion, generally falling into two categories: one is to limit motion to an acceptable range and adjust treatment margins accordingly, the other is to track and respond to the motion in real time. The former includes techniques such as abdominal compression, although the success of this technique for abdominal cancers is inconsistent (Van Gelder *et al*

2018, Lovelock *et al* 2014, Eccles *et al* 2011) and there are studies showing counterproductive results cases for lung SBRT (Mampuya *et al* 2014).

Active strategies rely on in-treatment tumor localization and corresponding adaptation. The position monitoring can be done through the use of an external or internal surrogate, or through some form of imaging (kV, MV, MR or ultrasound (Mostafaei *et al* 2018)). These methods of tumor tracking have been combined with beam gating (Berbeco *et al* 2005), or multi-leaf collimator (MLC) tracking (Keall *et al* 2000) to direct the correct dose to the target. However, the use of a surrogate either assumes or requires some modelling of the correlations between the surrogate and tumor motion, introducing additional uncertainties. Furthermore, the placement of external surrogates must be reproducible which is not guaranteed, and the implantation of internal surrogates, e.g. fiducials, can be limited by patient concerns (Scher *et al* 2019), indicating that a general motion management strategy relying solely on surrogates may not be attainable.

The use of imaging modalities to directly track tumor motion somewhat addresses uncertainty in modelling, however both ultrasound and kV imaging require some assumptions about tumor motion due to their relative orientations with respect to the beam. Utilising the MV on-board portal imager for tumor tracking removes these considerations entirely, while also adhering to AAPM goals to reduce imaging dose (Murphy *et al* 2007). The electronic portal imaging device (EPID) mounted on treatment linear accelerators collects images generated using the MV treatment beam. These beam's-eye-view (BEV) images are inherently of lower quality compared to kV images due to the physical processes that occur at higher energies. The higher noise and reduced contrast of MV images makes for a more challenging tracking environment, however previous work by our group demonstrates that tracking with these images is feasible to within 2 mm for 3D conformal lung treatments (Rottmann *et al* 2010) and continued development of EPID technology (Rottmann *et al* 2016) to improve photon detection efficiency indicate a promising future for MV tracking (Yip *et al* 2017).

In this paper we present a multi-region algorithm for markerless beam's-eye view tracking to enable tumor tracking during volumetric modulated arc therapy (VMAT) deliveries. This algorithm maintains the same advantages as previously discussed (adaptability to changing or irregular breathing patterns, robustness to target deformations) while removing the requirement of a training period and introducing tracking while the MLCs are in motion and/or the gantry is rotating.

2. Method

2.1. Algorithm overview
The tracking algorithm is built to automatically detect features of interest and track those features while visible within the aperture. To overcome the challenges of markerless tracking during treatments which include MLC and gantry motion, each feature that is identified for tracking is described by a cluster of templates generated along lines of high local variance. Template matching is performed on subsequent images using the calculated normalized cross-correlation (NCC) on the variance map of MV images to locate the template (image segment) on the image. The use of a cluster of templates serves two purposes; first it effectively encodes the shape of the feature, and second the reliance of only local information allows the tracker to adapt when features come in and out of view, or are lost, without impact on the tracking of other features. Tracking of a feature requires successful template matching of a majority of templates within the cluster, and preservation of the feature shape. An overview of the algorithm steps is shown in figure 1.

2.2. Image processing and aperture masking
To prepare each image for tracking, image smoothing and aperture masking are performed. Smoothing is performed through the application of a box filter and is required to reduce noise in the image and as well as limit the appearance of very small, high intensity features which may impede tracking. The aperture is masked through an adaptive thresholding algorithm, which separates foreground and background. The threshold is found through an iterative procedure which calculates the mean pixel value above and below the initial threshold, and adjusts this by the absolute difference in the calculated mean values until convergence. This algorithm was found to be successful for even complex apertures if the jaw positions are used to select a subsection of the image for processing.

The masking algorithm successfully detects the edge of the MLCs visible in the image, however further processing is required before tracking can be performed. The tracking algorithm first identifies regions of high variance and then tracks those features. The region close to the MLC edge, and hence close to the masked aperture edge, has a very high gradient in the image and so, without proper consideration, could result in inadvertent tracking of MLCs. To mitigate this, the aperture mask is narrowed to exclude the boundary gradient.
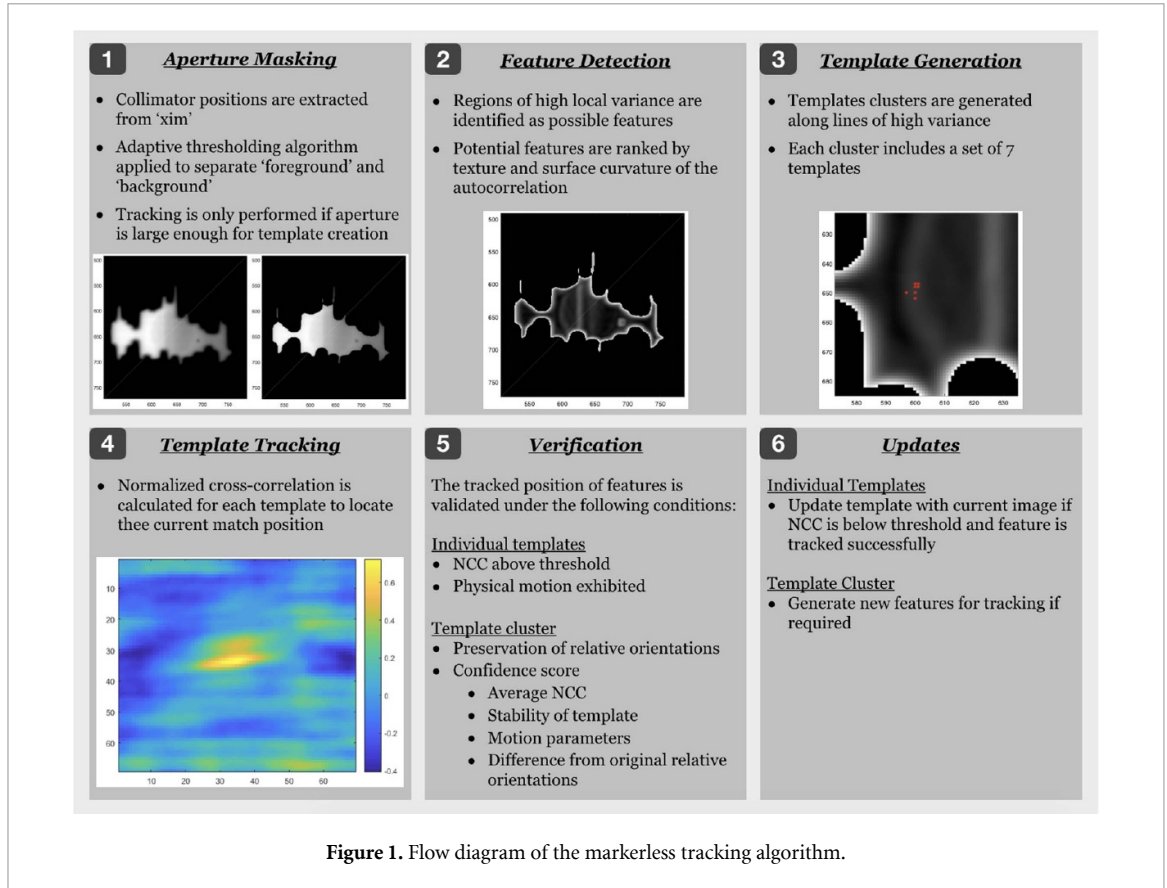
Figure 1. Flow diagram of the markerless tracking algorithm.

Template matching based tracking is limited to images where the aperture is open enough for templates to be generated (area > template size + exclusion region) so if this criteria is not met, the image is not processed and the algorithm progresses to the next. In addition, the number of tracked features is adapted to the aperture area.

2.3. Feature detection

A template matching based method relies on uniquely identifiable features in the templates to perform successful tracking. The initial selection of these features is done by ranking regions of high local texture. The local texture is computed by means of a local variance filter (Haralick [1979]) where the pixel value is set to the calculated local variance, as described in equation ([1]), where Q_{p_i} is a small region centered around the pixel p_i and containing M pixels. $\overline{Q}_{p_i}$ is the mean value of all pixels within Q_{p_i}. Once the highest texture values have been located (while satisfying minimum separation requirements from other features and the aperture boundaries) they are ranked by a score based on the texture value and the uniqueness of the feature parameterized by the autocorrelation value.

$$Var(Q_{p_i}) = \frac{1}{M-1}\sum (Q_{p_i}(x)) - \overline{Q}_{p_i})^2 \tag{1}$$

In comparison with previous work (Rottmann *et al* [2010]), a major change has been to absorb the pre-filtering of features into the main tracking procedure. The motivation for this adjustment is due to the dynamic nature of treatment types that are being targeted, which may not provide a stable and consistent set of images for pre-filtering. For the current implementation, if a feature is found to be static it is removed from the set of tracked features, and another is found to replace it using the same procedure outlined above.

2.4. Template creation

Previous versions of this tracking algorithm relied on the preservation of relative orientations of the features to make a determination on whether the feature had been reliably tracked or not. This approach works well for 3D conformal treatment plans but faces challenges for treatments with MLC or gantry motion. To resolve this, we generate a set of templates (each 21×21 pixels in size) in the region around each feature identified for tracking. The number of templates generated as part of a single cluster is 7, chosen to minimize computational cost while improving the stability of feature tracking. The locations of these templates are

determined by the path of the high local variance. This configuration allows us to infer the continued successful tracking of the feature based on the normalized cross-correlation values and relative orientation of these local templates, among other criteria, and also encodes information on the shape of the feature based on their orientation.

2.5. Template & feature tracking

Each feature is defined by a set of templates, the absolute position and relative orientations of which provide information that is used to determine whether or not a feature has been successfully tracked. The first step of this process is to calculate the new template positions using the 2D normalized cross-correlation of the templates with the current image. Next some selection criteria are applied to filter templates that have not been matched correctly, including a threshold on the normalized cross-correlation (0.5 for each template, 0.65 for the cluster average) and flagging templates that are static, where static templates are identified that have not moved more than one pixel per image for 5 images. An analysis is then performed of the relative orientations of the passing templates as follows. When the cluster of templates describing a single feature is created, a matrix encapsulating the position differences in each dimension between templates is calculated. On subsequent images, the absolute difference between the original matrix describing the relative orientations and the current matrix is examined. Each element is inspected in sequence, and if this element is above a predefined threshold (0.35 pixel) the contributing template is removed from the matrix and the difference comparison is restarted until all values are less than the threshold, resulting in a subgroup of templates that preserve their relative orientations. Subsequent to this, a recombination check is performed to see if any templates removed in the first run-through of comparisons also form a subgroup that would pass the relative orientation check. The reason for this is that there is no guarantee that the resulting group from the first run through of the relative orientation check successfully track the feature, so we introduce the recombination stage to address this possibility. The score of the subgroups is calculated as a weighted combination of the normalized cross-correlation value of the templates, divergence from the original relative orientations and the average stability of the templates in that group (how often they have contributed to successful feature tracking). Introducing a score at this stage ensures that features that are tracked are done so with a high level of confidence, and promotes the use of stable templates over the sequence of images.

2.6. Template updates and lost features

The final step of the tracking algorithm was introduced to improve tracking stability during VMAT treatments, where the perspective of the anatomy visible in the image is changing due to the rotating gantry. For features that are tracked successfully, with a high fraction of templates contributing to the matched position, the tracked templates are updated with the appropriate subsection of the current image. The cases where this update is performed are restricted to features where the confidence in the tracked position is high, avoiding the potential for templates to migrate to track an incorrect part of the anatomy.

2.7. Evaluation

To correctly evaluate the performance of the tracking algorithm, a set of images where the position of the tumor is known is required. Details of the equipment used to generate this set of images are provided in the following sections. The output of the tracking algorithm is backprojected to the isocenter plane and directly compared to the known tumor positions, projected onto the same plane. Histograms of the position differences in the x and y direction of the plane are generated and then fit with a normal distribution. The mean and width of the fit output are combined in quadrature to generate the tracking error in each direction of the 2D plane (referred to as 'x' and 'y'). These errors are combined, again in quadrature, to generate the final value for the tracking uncertainty.

Due to the nature of the treatment plan being delivered (VMAT), there may be periods of image acquisition where the tracking algorithm is not able to report a reliable tracked position. To quantify this a metric referred to as the tracking efficiency, the percentage of images reporting a successful tracked position, is evaluated and reported for each treatment field.

3. Experimental setup

3.1. Phantom data

To quantify the performance of the tracker a set of images is required with truth data for comparison with the tracker output. To create this dataset, images were collected of a dynamic thorax phantom (CIRS, Norfolk, VA, USA) containing a 2cm spherical tumor phantom (figure 2) in ciné mode by the EPID imager mounted on a Varian TrueBeam LINAC (Varian Medical System, Palo Alto, USA). Images were collected directly from the LINAC using the iTools Image Capture software (Varian Medical System, Palo Alto, USA)
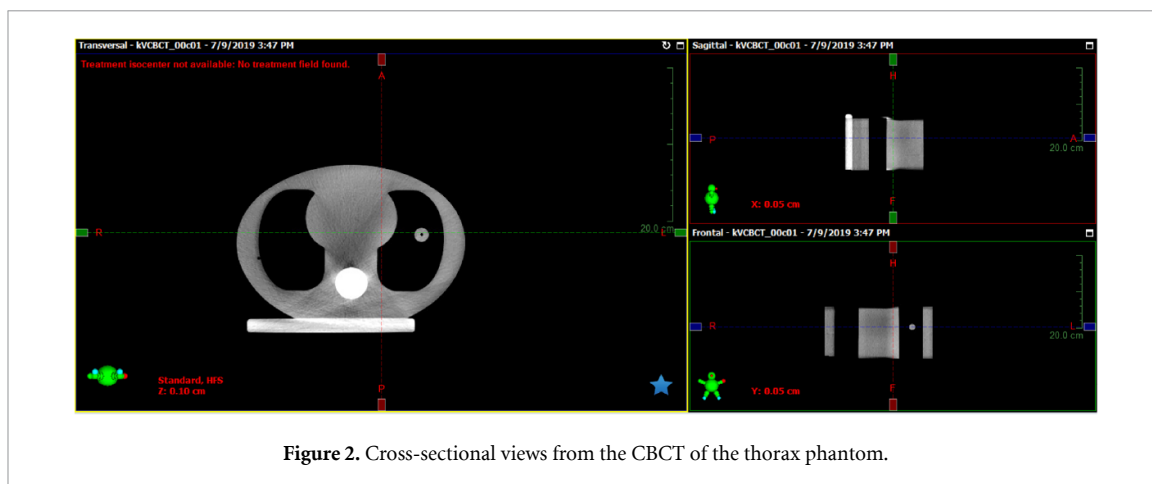
Figure 2. Cross-sectional views from the CBCT of the thorax phantom.

Table 1. Parameters of the delivered treatment plan.

Field	Beam Energy	Gantry Rtn	Coll Rtn	Couch Rtn	MU
1	6x FFF	20 CW 179	90	0	2479
2	6x FFF	179 CCW 20	5	0	2552
3	6x FFF	20 CW 179	355	0	2427

and stored in 'xim' format. The acquired image size is 1280×1280 pixels at intervals of approximately 0.1 seconds. The SID (source to imager distance) is set to 150 cm for the phantom images and 180 cm for all patient images, resulting in a spatial resolution of 0.219 mm and 0.183 mm respectively.

The delivered treatment plan was adapted, without re-optimization, from the SBRT plan of a lung patient and consists of 3 VMAT arcs, covering 160 degrees each, delivering a total dose to the target volume of 1800 cGy. A table summarising the parameters of each arc is shown in table 1.

To demonstrate the performance of the tracker in a more realistic scenario, the programmed motion of the phantom was modelled on patient breathing traces collected using an external sensor placed on the patients' chest during treatment (Varian RGSC system). These data were collected in the clinic during lung SBRT treatments and the traces from 3 patients were used to drive the motion of the phantom in turn. The phantom was set up to replicate the positioning of a patient on the couch during treatment, so the displacement axis of the internal cylinder of the phantom generates the superior-inferior (SI) motion, and the rotation axis of the cylinder generates both the left-right (LR) and anterior-posterior (AP) motion. To map the patient breathing trace onto these two degrees of freedom, the amplitude of the target SI motion is scaled to the extent of motion observed on the patients' 4DCT. The LR trace is similarly scaled by the amplitude of the tumor LR motion and used to program the rotation of the cylinder. The resulting motion extracted from the 3 breathing traces are shown in figure 3.

3.2. Patient data

To illustrate the portability of the tracker from phantom to patient data, images were collected during a lung SBRT treatment on a Varian TrueBeam LINAC (Varian Medical System, Palo Alto, USA). The lesion is located in the upper right lung, and is approximately 3.5 cm, 3 cm and 3 cm in diameter in the SI, LR and AP dimensions (figure 4). The patient's 4DCT showed a range of motion of approximately 8 mm, 3 mm and 6 mm in the SI, LR and AP directions respectively. The images were collected in the same manner as for the phantom images; the MV panel was extended during treatment delivery and images were collected in ciné mode by the EPID imager using the iTools Image Capture software (Varian Medical System, Palo Alto, USA).

4. Results

The markerless tracking algorithm was run retrospectively on MV images collected during the delivery of the previously described treatment plan to the dynamic thorax phantom. Three sets of images were recorded, corresponding to the delivery of the treatment plan to the phantom during the three separate patterns of programmed motion. To extract a quantitative metric for the tracking uncertainty, the tracked displacement of features from the images must be compared to the expected motion. This comparison is performed at the isocenter plane orthogonal to the central axis of the treatment beam. The 3D motion generated by the displacement and rotation of the cylinder within the dynamic phantom is projected to a pixel position on the
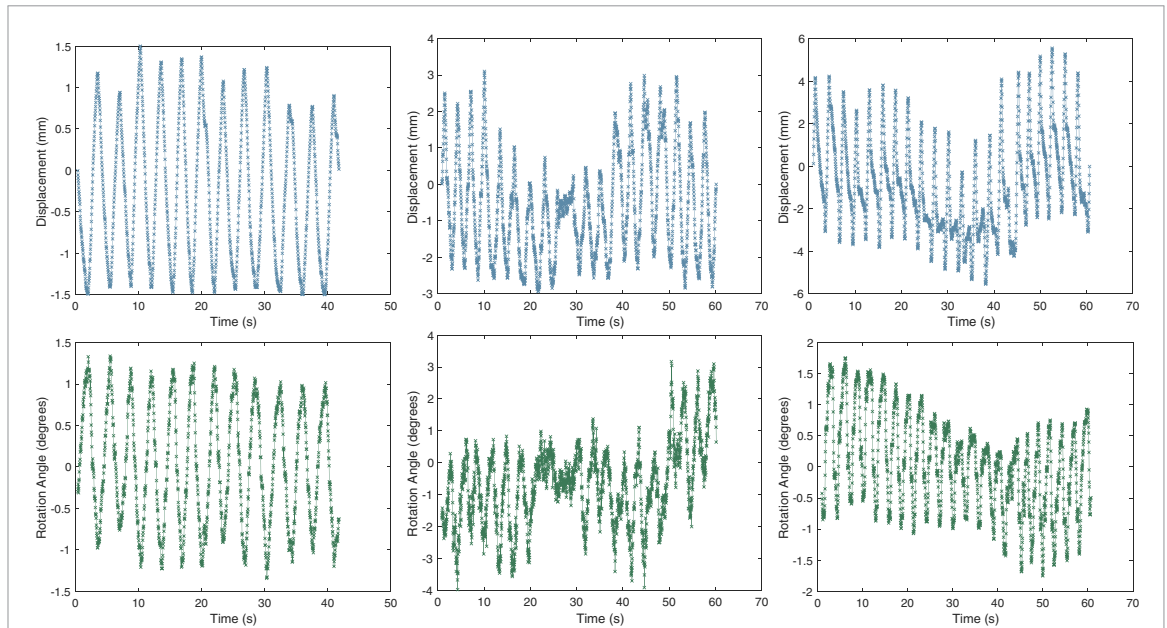
Figure 3. Programmed displacement (top row) and rotation (bottom row) of the dynamic thorax phantom mapped from the breathing traces of three lung SBRT patients.
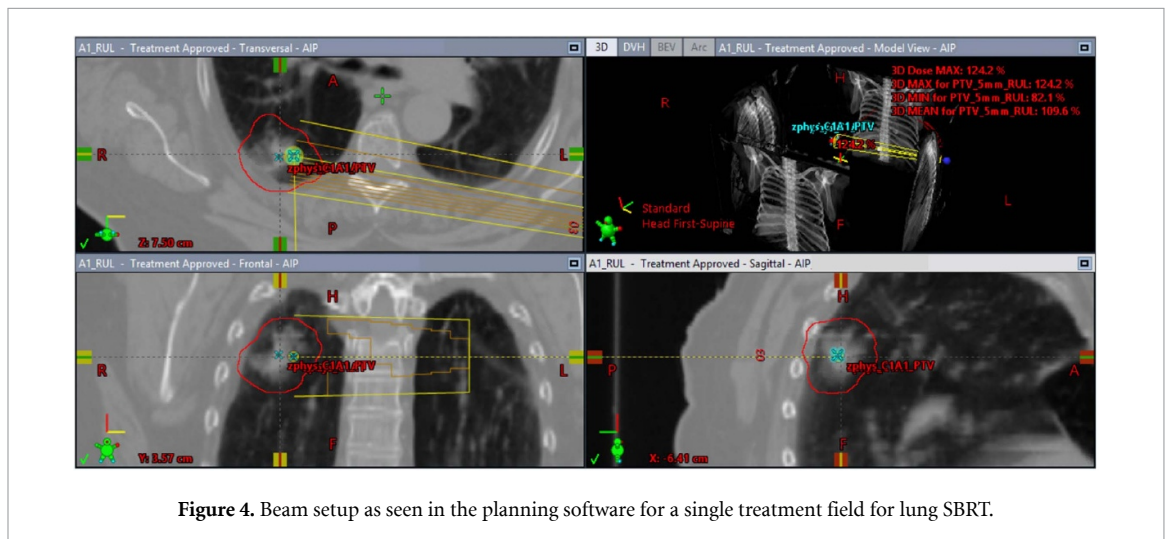

Figure 4. Beam setup as seen in the planning software for a single treatment field for lung SBRT.

MV imager, and then backprojected to the isocenter plane, allowing for a direct comparison of displacement values. An example of the tracker output in comparison to the projected phantom motion is shown in figure 5.

Due to the interference between the aperture size, position and shape, gantry angle and the motion of the tumor phantom itself the average tracking efficiency (number of images out of the series, roughly 1200 images, which generated a tracking output) is low and was found to be 16%, 8% and 8% for the first, second and third treatment fields respectively. There are parts of the image sequences in which the tumor is not visible, either due to mismatch of the aperture position and the tumor position at that time, or the aperture is not large enough for the tumor to be visible. Thus when tracking is re-established, the displacement centre for that track is set to zero. In order to make a comparison between external information and the tracked positions, the origins of the two coordinate systems must be aligned. To do this we seed the initial track offset by the value of the function describing the tumor motion at that time. The data points used to align the coordinate origins are not used in the evaluation.

The tracking error is evaluated using the method described in 2.7. This was initially performed separately for each delivered treatment field to check for any trends in the uncertainty based on the phantom motion and was performed for the full data set together to measure the total uncertainty (figure 6).

The tracking errors resulting from the fit to the difference histograms are summarised in table 2. For each treatment field the total error is less than 1.5 mm, and the total tracking error was found to be 1.34 mm.
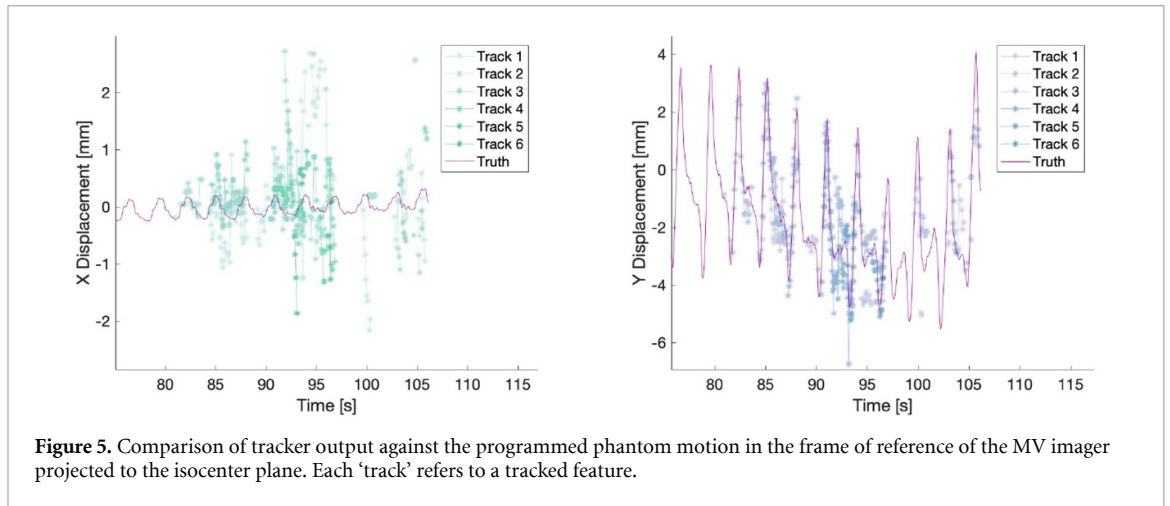
Figure 5. Comparison of tracker output against the programmed phantom motion in the frame of reference of the MV imager projected to the isocenter plane. Each 'track' refers to a tracked feature.
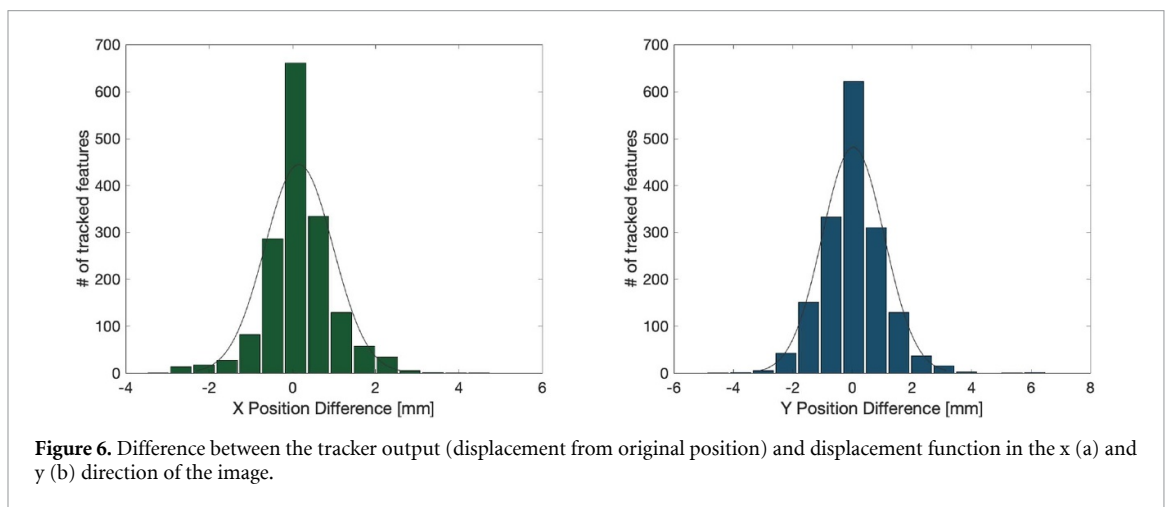

Figure 6. Difference between the tracker output (displacement from original position) and displacement function in the x (a) and y (b) direction of the image.

Table 2. Tracking error summary table. The tracking error is broken down for each patient trace used, field and dimension on the imager plane at ISO. The 95% error is the value under which 95% of the data points fall and the % tracked describes the percentage of images that reported a successful track.

	Error (mm)									
	Trace 1			Trace 2			Trace 3			
Field	1	2	3	1	2	3	1	2	3	Total
X	0.52	0.98	0.82	0.69	1.20	1.16	0.77	1.00	1.14	–
Y	1.18	1.01	0.50	1.2	0.93	0.68	1.00	0.72	1.41	–
Total	1.29	1.41	0.97	1.38	0.97	1.34	1.26	1.23	1.81	**1.34**
95% Error	2.71	2.62	1.88	2.54	2.43	2.52	2.46	2.38	3.53	2.64
% Tracked	15.7	9.3	7.6	15.7	7.6	6.7	17.5	8.8	8.9	10.9

4.1. Patient data example

We applied the tracking algorithm to MV image data acquired during a lung SBRT treatment. A section of 60 images was chosen, sufficient to cover a full breathing cycle. Two example MV images are shown in figure 7. The example images (left/middle of figure 7) show two MV frames separated by approximately 1 second. Each tracked feature is indicated as the cluster of template positions, which are highlighted as magenta or red depending on whether the individual templates have been successfully tracked or not. The cyan arrows indicate the position relative to the original template location. Tracking was successful on 80% of the images, with majority of cases where tracking was lost being only for a single image, and the maximum period tracks were lost for was over 3 consecutive images (approximately 0.3 seconds). For this example, extracting the delivered dose from the image 'xim' files and summing over images where a track was not reported, the number of MU delivered in that period was 15 MU.
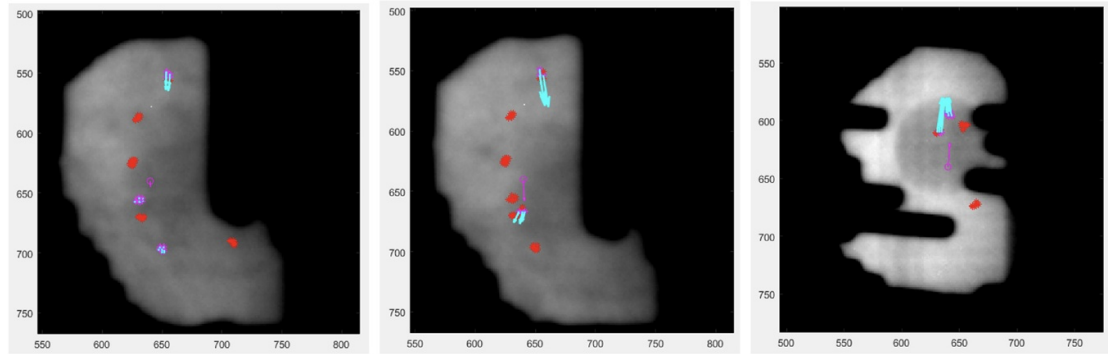
Figure 7. Screenshots of tracking output on patient data approximately a second apart (left and middle). The RHS plot is an example of tracking on the phantom data. The crosses indicate the original feature position (magenta if tracked, red if previously tracked but lost on the current image) and the cyan arrows indicate the current tracked position.
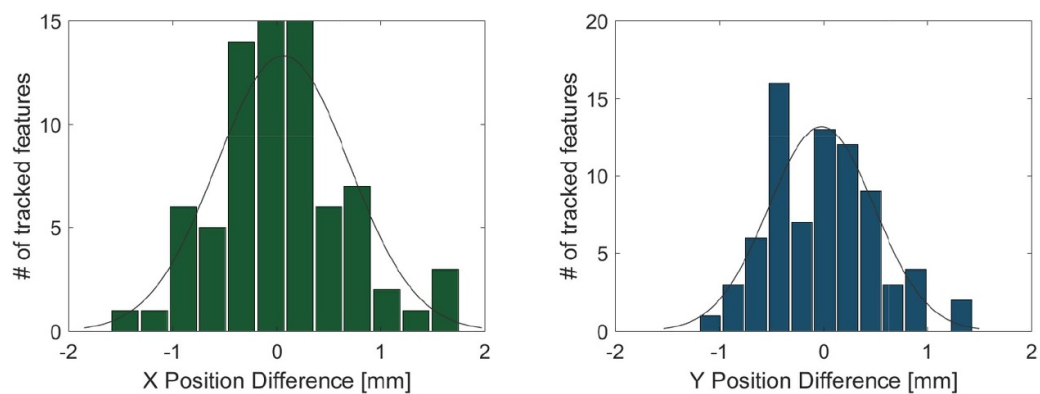

Figure 8. Difference between the tracker output (displacement from original position) and manually tracked positions in the x (a) and y (b) direction of the image.

To estimate the tracking error, the output was compared to manually tracked positions. As the features are allowed to move independently, this was performed on a feature-by-feature basis. To track manually, a dedicated template is created at the feature location on the image where the feature is generated by the tracker. An expert then submits a match position for the template on subsequent images, until the template can no longer be matched successfully. The difference between the manually tracked position and the output of the tracker is computed. The histogram of these difference values is used to calculate the tracking performance. The same procedure as for the tracker output was followed to evaluate the tracking performance, and the fit to the histograms to generate the error in the x and y plane of the MV panel are shown in figure 8. The resulting tracking uncertainty from the evaluation of these 60 images was 0.68 mm.

5. Discussion

Tumor tracking based solely on MV images is a challenging task. Our approach to this challenge is conservative, with mechanisms in place to ensure tracking is only reported when there is confidence that the feature is tracked successfully. This reduces the tracking efficiency in terms of the number of images out of the total collected during the treatment field delivery that reported a tracked feature. In particular, for the images collected for this study, the imaging table installed on the couch creates a lattice effect on the MV images that moves as the gantry rotates. Creating a template on these grid lines introduces the possibility that the tracking would follow the gridlines rather than the intended target. To address this, we have introduced masking of vertical lines in the images, which reduces the tracking area available. This issue will be resolved in the future by a new imaging couch that does not produce a grid pattern on images.

Contributing to the low number of images that successfully produce tracks is the phantom itself, which is relatively homogeneous compared to real patient anatomy. This results in templates created mainly on the boundary between the phantom tumor and the surrounding material. Whereas tracking on real anatomy benefits from the texture of adjacent tissues, providing a larger region during MLC motion will present more availability of unobscured, trackable regions.

In comparison to the tracking error observed from the phantom images, our initial evaluation using a subset of images from an SBRT lung treatment demonstrates a lower value for the tracking error. We believe this is due to the type of phantom used for the study, in particular the shape of the tumor phantom. The size of each individual template is 19 x 19 pixels, which is 3.47 mm in the isocenter plane. The tumor phantom is a sphere of 2 cm diameter. Templates are created along the edge of the tumor phantom insert, because they generate smooth lines of high variance. The smoothness of these lines and the homogeneity of the material results in the generated templates being centered on features that are not fully unique, and the templates can match on regions slightly above or below the initiated point on the edge of the sphere with high confidence, potentially resulting in an increased tracking uncertainty.

Currently our tracking algorithm is applied retrospectively to series of images, and tracking on each image is completed in approximately 0.2 seconds, longer than required for running on real-time images (collected each 0.1 seconds, although this does not include any additional time required for transferring the image or accessing it through the API). However, there is room to improve by streamlining some of the processing, for example, when performing the normalized cross-correlation calculation for template matching some calculations are included to ensure any MLC boundaries and the image region beyond this to not contribute to a match. These calculations could be moved up a level in the structure so they are performed on a per-image basis. In addition, profiling the code shows there are instances where functions are repeated, which could be solved by passing information rather than recalculating. Finally, the computer being used contains an Intel ES-1630 CPU (2014), which is outperformed by CPUs found in newer PCs. Considering these factors we believe the algorithms will perform tracking at a rate fast enough to implement real-time tracking.

A review of the literature reveals a range of approaches to tracking on MV images including single template matching (Arimura *et al* 2009) and registration of simulated MV digitally reconstructed radiographs (DRRs) (Rozario *et al* 2018) which track tumor position with an uncertainty of 1.47 ± 0.60 mm and 0.98 mm respectively, and a machine learning approach (Tang *et al* 2009) to detect when the tumor is outside of the aperture. The tracking uncertainty reported here is comparable to these values, and also to our group's previously published algorithm (Rottmann *et al* 2010) as well as markerless tracking algorithms utilising alternative sources of information, for example, on-board kV images (Hazelaar *et al* 2018).

Furthermore, to our knowledge this is the first presentation of markerless tracking using MV images collected during the delivery of a VMAT treatment. The demonstration of this tracking algorithm on phantom and an example patient data shows that this approach is feasible for complex delivery techniques with low tracking uncertainty. The previous functionality of the tracking algorithm has been preserved, and indeed should be improved by the template update process in reaction to inflating and deflating lungs. As an aside, by introducing feature recognition at the template generation stage, this algorithm can also be used for fiducial tracking. Further validation on a large clinical data set is required to fully explore the advantages and limitations of this method. Once the verification against the clinical data has been performed, an investigation towards clinical implementation of the tracking algorithm can be explored, building on previous work performed by our group investigating the use of a combined tracking and prediction algorithm to perform MLC tracking (Rottmann *et al* 2014).

6. Conclusion

An algorithm has been developed to perform markerless tumor tracking on MV ciné EPID images collected during VMAT treatments. The tracking uncertainty of this algorithm was evaluated with a dynamic thorax phantom programmed with motion derived from patient traces. The reported tracking error is 1.34 mm, comparable to previously reported tracking errors by our group on 3D conformal treatments. Further studies will confirm the accuracy on a large clinical data set.

Acknowledgment

References

Arimura H *et al* 2009 Computerized method for estimation of the location of a lung tumor on EPID cine images without implanted markers in stereotactic body radiotherapy *Phys. Med. Biol.* **54** 665–77

Berbeco R I, Nishioka S, Shirato H, Chen G T Y and Jiang S B 2005 Residual motion of lung tumours in gated radiotherapy with external respiratory surrogates *Phys. Med. Biol.* **50** 3655–67

Eccles C L, Patel R, Simeonov A K, Lockwood G, Haider M and Dawson L A 2011 Comparison of liver tumor motion with and without abdominal compression using cine-magnetic resonance imaging *Int. J. Radiat. Oncol. Biol. Phys.* **79** 602–8

Ekberg L, Holmberg O, Wittgren L, Bjelkengren G and Landberg T 1998 What margins should be added to the clinical target volume in radiotherapy treatment planning for lung cancer? *Radiother. Oncol.* **48** 71–7

Haralick R 1979 Statistical and structural approaches to texture *Proc. IEEE* vol **67** pp 786–804

Hazelaar C, Dahele M, Mostafavi H, van der Weide L, Slotman Band Verbakel W 2018 Markerless positional verification using template matching and triangulation of kV images acquired during irradiation for lung tumors treated in breath-hold *Phys. Med. Biol.* **63** 115005

Katoh N *et al* 2008 Real-time tumor-tracking radiotherapy for adrenal tumors *Radiother. Oncol.* **87** 418–24

Keall P J *et al* 2006 The management of respiratory motion in radiation oncology report of aapm task group 76a) *Med. Phys.* **33** 3874–900

Keall P J, Kini V R, Vedam S S and Mohan R 2000 Motion adaptive x-ray therapy: a feasibility study *Phys. Med. Biol.* **46** 1–10

Kitamura K *et al* 2002 Three-dimensional intrafractional movement of prostate measured during real-time tumor-tracking radiotherapy in supine and prone treatment positions *Int. J. Radiat. Oncol.* **53** 1117–23

Liang Z, Liu H, Xue J, Hu B, Zhu B, Li Q, Zhang S and Wu G 2018 Evaluation of the intra- and interfractional tumor motion and variability by fiducial-based real-time tracking in liver stereotactic body radiation therapy *J. Appl. Clin. Med. Phys.* **19** 94–100

Lovelock D M, Zatcky J, Goodman K and Yamada Y 2014 The effectiveness of a pneumatic compression belt in reducing respiratory motion of abdominal tumors in patients undergoing stereotactic body radiotherapy *Technol. Cancer Res. T.* **13** 259–67

Mampuya W A *et al* 2014 The impact of abdominal compression on outcome in patients treated with stereotactic body radiotherapy for primary lung cancer *J. Radiat. Res.* **55** 934–9

Mostafaei F, Tai A, Gore E, Johnstone C, Haase W, Ehlers C, Cooper D T, Lachaine M and Li X A 2018 Feasibility of real-time lung tumor motion monitoring using intrafractional ultrasound and kv cone beam projection images *Med. Phys.* **45** 4619–26

Murphy M J *et al* 2007 The management of imaging dose during image-guided radiotherapy: Report of the aapm task group 75 *Med. Phys.* **34** 4041–63

Rottmann J, Aristophanous M, Chen A, Court L and Berbeco R 2010 A multi-region algorithm for markerless beam's-eye view lung tumor tracking *Phys. Med. Biol.* **55** 5585–98

Rottmann J, Keall P and Berbeco R 2014 Markerless EPID image guided dynamic multi-leaf collimator tracking for lung tumors *Phys. Med. Biol.* **58** 4195–204

Rottmann J, Morf D, Fueglistaller R, Zentai G, Star-lack J and Berbeco R 2016 A novel EPID design for enhanced contrast and detective quantum efficiency *Phys. Med. Biol.* **61** 6297–306

Rozario T, Chiu T D, Chen M, Jia X, Lu W, Bereg S and Mao W 2018 A novel markerless lung tumor-tracking method using treatment MV beam imaging *Appl. Sci.* **8** 2525

Scher N *et al* 2019 Safety and efficacy of fiducial marker implantation for robotic stereotactic body radiation therapy with fiducial tracking *Radiat. Oncol.* **14** 167

Seppenwoolde Y, Shirato H, Kitamura K, Shimizu S, van Herk M, Lebesque J V and Miyasaka K 2002 Precise and real-time measurement of 3d tumor motion in lung due to breathing and heartbeat, measured during radiotherapy *Int. J. Radiat. Oncol.* **53** 822–34

Tang X, Lin T and Jiang S 2009 A feasibility study of treatment verification using EPID cine images for hypofractionated lung radiotherapy *Phys. Med. Biol.* **54** S1–S8

Van Gelder R, Wong S, Le A, Podreka A, Briggs A, Haddad C and Hardcastle N 2018 Experience with an abdominal compression band for radiotherapy of upper abdominal tumours *J. Med. Radiat. Sci.* **65** 48–54

Yip S S, Rottmann J, Chen H, Morf D, Füglistaller R, Star-Lack J, Zentai G and Berbeco R 2017 Technical note: Combination of multiple epid imager layers improves image quality and tracking performance of low contrast-to-noise objects *Med. Phys.* **44** 4847–53

2.2 Clinical translation of a new flat-panel detector for beam's-eye-view imaging

The manuscript reproduced in this section presents the results of the initial measurements made with the prototype EPID. First, we conducted a suite of standard imaging performance tests, including modulation transfer function (MTF), noise power spectrum (NPS), detective quantum efficiency (DQE), contrast-to-noise ratio (CNR), signal-to-noise ratio (SNR), and linearity with dose.

MTF is a quantitative description of the spatial resolution of an imaging system. It can predict the imaging response to objects of a range of sizes, commonly measured experimentally (Fujita *et al.* 1992). NPS is a measure of the noise characteristics of an imaging system at all spatial frequencies, that is also determined experimentally (IEC 2003). DQE combines the spatial resolution and noise characteristics of an imaging system to describe how effectively a detector can produce a high SNR image relative to an ideal detector. DQE at any spatial frequency is calculated by the following equation:

$$DQE(f) = \frac{|MTF(f)|^2}{(q \cdot nNPS(f))}$$

Where q is the incident photon fluence and nNPS is the normalized NPS. CNR evaluates contrast and estimates the noise of an image by taking the ratio of the difference between the signal in a region of interest and the background noise. SNR is a related metric that examines the signal directly. Linearity tests verify that the response of a detector is linear to the amount of incident radiation.

The results were compared to the analogous parameters for standard single layer imager. The novel panel was then tested on an anthropomorphic phantom in order to assess its potential response when imaging human anatomy. Finally, the panel was tested on actual human anatomy, using preliminary patient data acquired for the study presented in chapter 2.3. In

each test the MLI was found to be a substantial improvement over a single layer flat panel.

The thesis author designed this series of experiments with support from his co-authors.   He collected and analyzed all the data.   He also prepared the manuscript describing the findings.

Physics in Medicine & Biology

IPEM Institute of Physics and Engineering in Medicine

PAPER

Clinical translation of a new flat-panel detector for beam's-eye-view imaging

TC Harris[1,2,3], J Seco[2,3], D Ferguson[1], M Lehmann[4], P Huber[4], M Shi[1,5], M Jacobson[1], I Valencia Lozano[1], M Myronakis[1], P Baturin[6], R Fueglistaller[4], D Morf[4] and R Berbeco[1]

[1] Department of Radiation Oncology, Dana Farber/Brigham and Women's Cancer Center, Harvard Medical school, Boston, MA, United States of America
[2] BioMedical Physics in Radiation Oncology, DKFZ, Heidelberg, Germany
[3] Department of Physics, University of Heidelberg, Heidelberg, Germany
[4] Varian Medical Systems, Baden-Dattwil, Switzerland
[5] University of Massachusetts Lowell, Lowell, MA, United States of America
[6] Varian Medical System, Palo Alto, CA, United States of America

E-mail: tharris@bwh.harvard.edu

Keywords: MV imaging, DQE, clinical translation

Abstract

Electronic portal imaging devices (EPIDs) lend themselves to beams-eye view clinical applications, such as tumor tracking, but are limited by low contrast and detective quantum efficiency (DQE). We characterize a novel EPID prototype consisting of multiple layers and investigate its suitability for use under clinical conditions. A prototype multi-layer imager (MLI) was constructed utilizing four conventional EPID layers, each consisting of a copper plate, a Gd2O2S:Tb phosphor scintillator, and an amorphous silicon flat panel array detector. We measured the detector's response to a 6 MV photon beam with regards to modulation transfer function, noise power spectrum, DQE, contrast-to-noise ratio (CNR), signal-to-noise ratio (SNR), and the linearity of the detector's response to dose. Additionally, we compared MLI performance to the single top layer of the MLI and the standard Varian AS-1200 detector. Pre-clinical imaging was done on an anthropomorphic phantom, and the detector's CNR, SNR and spatial resolution were assessed in a clinical environment. Images obtained from spine and liver patient treatment deliveries were analyzed to verify CNR and SNR improvements. The MLI has a DQE(0) of 9.7%, about 5.7 times the reference AS-1200 detector. Improved noise performance largely drives the increase. CNR and SNR of clinical images improved three-fold compared to reference. A novel MLI was characterized and prepared for clinical translation. The MLI substantially improved DQE and CNR performance while maintaining the same resolution. Pre-clinical tests on an anthropomorphic phantom demonstrated improved performance as predicted theoretically. Preliminary patient data were analyzed, confirming improved CNR and SNR. Clinical applications are anticipated to include more accurate soft tissue tracking.

1. Introduction

Electronic portal imaging devices (EPIDs) provide an efficient method of radiotherapy verification and localization (Herman *et al* 2001). Initially used as a replacement for film cassettes in the acquisition of MV portal images, other clinical uses for EPIDs have since been developed. EPID use as a pretreatment QA tool has been reported for intensity-modulated radiotherapy (Warkentin *et al* 2003, Fuangrod *et al* 2014) and volumetric modulated arc therapy (VMAT) plans (Bakhtiari *et al* 2011, Woodruff *et al* 2013). In addition, EPIDs have been shown to aid in treatment delivery QA (Partridge *et al* 2002, Wendling *et al* 2009). *In vivo* dosimetry with an EPID verifies that a treatment plan is being delivered as intended, or monitors anatomical changes that might lead to a deviation in the intended dose distribution (Nijsten *et al* 2007, Celi *et al* 2016). An EPID-based *in vivo* system provides speed and ease of use compared to some alternatives, because the

entire radiation field is sampled at a high resolution rather than discrete points, and do not require additional detectors such as MOSFETs or optically stimulated luminescence dosimeters.

When operated in 'cine mode', an EPID acquires sequential images from the MV beam, capturing the fluence of a treatment field after traversing a patient. This real-time functionality has led researchers to investigate applications such as treatment verification and monitoring. As an example, MV cine has been used to monitor deep inspiration breath hold (DIBH) procedures to verify the reduction of cardiac dose for left breast radiation treatments (Jensen *et al* 2014). Tumor motion quantification (Ueda 2012), tumor tracking (Rottmann *et al* 2013b, Ferguson *et al* 2020), and multi-leaf collimator (MLC) adaptation to tumor motion (Rottmann *et al* 2013a) have all been shown to be feasible using MV cine imaging.

MV cine imaging has several benefits compared to on-board orthogonal kV imaging. Foremost, there is no extra imaging dose to the patient. For real-time applications, continuous kV fluoroscopy dose can become non-negligible. In addition, the MV cine images display the actual anatomy receiving radiation, as it is being irradiated, rather than an orthogonal image of arbitrary size. Each individual MV frame is 2D, but the third dimension, depth, is dosimetrically not as important for high energy x-ray irradiation. Despite these advantages, clinical implementation of EPIDs in advanced motion management has been limited by several factors, including the inherent low contrast of MV imaging and the relatively low detective quantum efficiency (DQE) of currently commercially available EPIDs (Antonuk 2002).

The internal structure of most current EPIDs in clinical use includes three main components. (1) A copper sheet that acts as a buildup layer to convert photons into secondary electrons, as well as a shield against low energy scattered radiation. (2) A scintillation material, typically terbium doped gadolinium oxysulfide (GOS), to convert radiation to optical photons. (3) Hydrogen doped amorphous silicon deposited on a glass substrate to form a pixelated array of photodiode thin film transistors to detect the optical photons (Street *et al* 1990, Antonuk *et al* 1990, Munro and Bouius 1998). While resistant to radiation damage and cost effective to manufacture, these EPIDs typically have a DQE(0) of about 1%–2% at MV energies (El-Mohri *et al* 2001).

Considerable research has been devoted to improving EPIDs, in order to support advanced clinical applications. Investigators have explored different scintillation materials (Hu *et al* 2019), pixelated scintillators (Star-Lack *et al* 2015), and structured phosphors (Zhao *et al* 2004), for example. A cost-effective and easily implementable approach is to stack multiple layers of currently available components to improve photon collection without increasing Swank noise (Swank 1973). This multi-layer approach can preserve spatial resolution and field of view, while providing a substantial increase in DQE. This concept was first explored using commercially available parts manually adapted to a four-layer configuration (Rottmann *et al* 2016). The prototype was the subject of several preliminary investigations of tumor tracking (Yip *et al* 2017), spectral imaging (Myronakis *et al* 2017) and tracking fiducials behind MLCs (Hu *et al* 2018b), for example. One major drawback was that this design suffered from high noise and unstable behavior due to thermal issues. Drawing from the lessons of the previous experience, the detector described in the current study was designed from the ground up, featuring improved electronics to reduce thermal noise and to enable easy clinical deployment in place of the standard EPID. The simpler stackup of electronic boards is a novel strategy which will readily permit swapping of different layers of varying thickness or material and comparing their performance in future studies. This new multi-layer imager (MLI) prototype was characterized and compared to a stock AS-1200 EPID (Varian Medical systems, Inc). Pre-clinical tests were performed with anthropomorphic phantoms and the MLI mounted on the linac gantry in place of the standard imager. Finally, initial beam's-eye-view patient data were acquired during radiotherapy treatments and detector performance evaluated for clinical applications.

2. Materials and method

The novel MLI prototype used in this study was constructed at Varian's Imaging Laboratory in Baden, Switzerland. The MLI does have certain similarities to the AS-1200. They both have an active area of 43 cm × 43 cm, a pixel pitch of 0.336 mm, and a maximum frame rate around 25 Hz. However, in addition to having four layers of amorphous silicon photodiode arrays, the MLI utilizes a thicker scintillator compared to the AS-1200, 0.436 mm (200 mg cm^{-2}) × 4 layers versus 0.290 mm (113 mg cm^{-2}) × 1 layer. In addition, the MLI's electronics were re-designed and significantly altered to meet the challenge of fitting the additional layers into the same size housing as the AS-1200. In-house custom-built application-specific integrated circuits (ASICs) perform readout and digitization of the photodiodes. Each layer's response is averaged together. A field programmable gate array (FPGA) chip combines the digitized data before sending it to the host computer for further processing and display. In the currently deployed firmware, the individual layers are averaged vertically without any geometry compensation for the magnification change between layers. If needed, a combination of the four layers taking into account the relative rigid registrations between
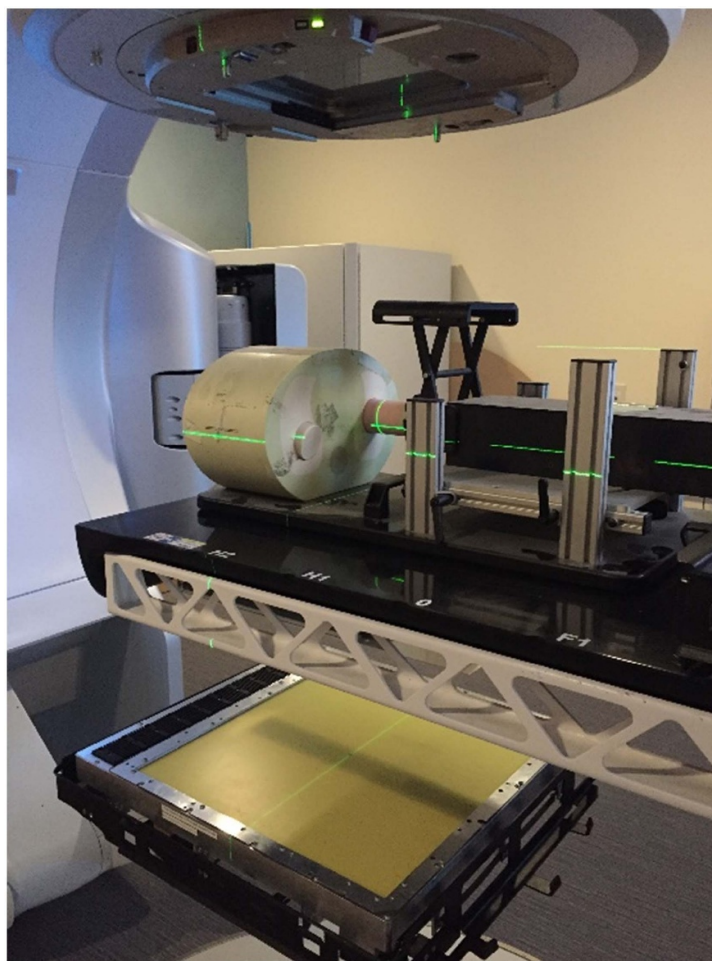
Figure 1. Multi-layer imager without its cover mounted on a TrueBeam. All measurements were taken with the imager in the same mount and housing as the standard EPID, as well as utilizing the same data chains.

layers could be deployed, but in practice the current simple solution provides sufficient spatial resolution (see section 3.2). Special consideration was given to cooling the readout ASICs and power supply board. Boards with aluminum cooling elements were inserted and transfer heat via thermal pads. These cooler elements are then air cooled by air flow, assisted by fans. The maximum temperature of the readout boards is 15 °C cooler than in previous prototypes, addressing noise and breakdown issues. Although the MLI fits in the same housing as the AS-1200, at 24.7 kg versus 18.0 kg, it weighs 6.7 kg more. To ensure the mounting arm could handle the additional load, Varian performed 10 000 test cycles of detector extension, gantry rotation, and detector retraction before releasing the EPID for clinical testing.

Measurements in this study were taken with a 6 MV beam from a Varian TrueBeam linac. The clinical images acquired during patient treatments were taken in flattening-filter-free mode. The beams were calibrated to deliver 1 cGy MU^{-1} in water at dmax of 1.5 cm, a 10 cm × 10 cm open field, at 100 cm SAD. A standard Varian AS-1200 was used as the reference imager. The prototype was mounted on a clinical linear accelerator (Varian Medical Systems, Inc) using the same collision frame and imager cover as the AS-1200 imager (figure 1) and utilizing the same clinical image acquisition chain.

2.1. Detector characterization

The linearity of detector response is important for quantitative applications, such as *in vivo* dosimetry. Detector response was measured up to saturation for the MLI all layers combined, the MLI top layer only, and the reference AS-1200 detector. Images were taken at 140 cm source-to-imager distance (SID) with a 15 cm × 15 cm field size, flattening filter in, and no flood field, dark field, or dead pixel corrections. No post-processing of any kind was used. Ten frames were collected at 10 frames per second in ad hoc high resolution mode for each MU settings, and the MU exposure in the image header was recorded. The average pixel value of the central 240 × 240 pixel region was determined.

Contrast and noise are two metrics commonly used to describe image quality. Contrast-to-noise ratio (CNR) evaluates the degradation of contrast and estimates the noise of an image by taking the ratio of the

difference between the signal of two regions of interests and the background noise. Signal-to-noise ratio (SNR) is a related metric that examines the signal directly.

CNR and SNR were measured on a Las Vegas contrast phantom. The phantom was placed drilled holes-side down on the treatment couch, and isocenter was placed at the couch surface. Each image was acquired with 1 MU, flattening filter in, at 150 cm SID. The signal was taken to be a circular region in the hole marked in figure 3, and background was an annulus surrounding the hole. Prior to making region of interest (ROI) noise calculations, a median filtered version of the image was subtracted from the original image, so as to remove deterministic background non-uniformities from the ROI. A 5×5 median pixel filter window was used for this step, which outputs the median pixel value in a 5×5 pixel neighborhood around the input pixel. This was done only as part of CNR and SNR calculation steps (as well as the CNR/SNR analysis for the pre-clinical and clinical data), and not for noise power spectrum (NPS) or DQE. CNR and SNR were calculated according to the equations below.

$$CNR = \frac{(S_{in} - S_{out})}{\sqrt{\sigma_{in}^2 + \sigma_{out}^2}} ; SNR = \frac{S_{in}}{\sigma_{out}}$$

Where S_{in} is the mean response of the circular region, S_{out} is the mean response of the annulus background region, σ_{in} is the standard deviation of the circular region, and σ_{out} is the standard deviation of the background signal.

The spatial resolution of an imaging system is often described quantitatively by the modulation transfer function (MTF). This metric describes the behavior of spatial resolution for a range of spatial frequencies, and can be used to predict the imaging performance of objects of a corresponding range of sizes. The MTF can be obtained experimentally by imaging a setup that yields a line spread function (LSF). Calculation of the Fourier transform of the LSF generates the MTF. This study followed the method by Fujita *et al* (1992). In short, a LSF was created by utilizing a pair of heavy tungsten blocks (12 cm $\times$ 7.7 cm $\times$ 18.7 cm) separated by 100 μm shims to create a slit. The central axis of radiation was aligned with the slit, the imager was placed at 150 cm SID, the couch was angled 2°, and 200 frames were averaged. The Fourier transform was calculated using Matlab FFT routines.

Detectors experience noise related to the quantum nature of the incident photons. CNR and SNR estimate noise by the standard deviation of pixel values in a region. The NPS is a comprehensive metric that measures the noise characteristics of a system at all spatial frequencies, providing a complete description of an imager's noise profile. NPS is best measured by flood field images close to saturation of the detector so that noise associated with the readout electronics is small in comparison. Our study acquired 200 10 cm $\times$ 10 cm flood field images at around 70% saturation. Frames were detrended by subtracting the average of 200 images. Following the International Electrotechnical Commission (IEC 2003) procedure, a central 120×120 pixel^2 region was processed to create a 2D normalized NPS (nNPS). The first ten rows on either side of the zero-frequency axis were averaged to create the 1D nNPS. This procedure was done with the full MLI, top layer-only MLI, and the reference detector (AS-1200).

The DQE combines the effects of signal and noise performance of an imaging system as a function of spatial frequency. It describes how effectively the system can produce a high SNR image relative to an ideal detector. An ideal detector has a DQE of 11.0 or 100%, meaning all the radiation energy absorbed is converted into image information. High DQE values indicate that less radiation is needed to achieve identical image quality. The DQE of a system is given by:

$$DQE(f) = \frac{|MTF(f)|^2}{(q \cdot nNPS(f))}$$

where f is the spatial frequency and q is the incident photon fluence. The average photon fluence for SID $r_o = 100$ cm was simulated by Monte Carlo for the linac to be $q_o = 1.42 \times 10^7$ photons cGy mm^{-2} (Star-Lack *et al* 2014). An inverse square correction was then applied such that $q = q_o \cdot r_o^2 / r^2$.

2.2. Phantom study

An anthropomorphic thorax phantom with an embedded lung tumor model was setup head-first supine on the treatment couch with isocenter placed in the center of the tumor. The MV imager (MLI or AS1200) was set to 150 cm SID. A 1 MU single frame image was taken with the 6 MV beam with flattening filter at gantry angles 0 and 270 degrees (anteroposterior (AP) and right lateral) with the MLI in 4- and 1-layer modes, and with the reference detector (AS-1200). Images had flood field, dark field, and pixel map corrections. The CNR and SNR were calculated on the AP view using the tumor as signal and an area in the lung as background. A 5×5 median pixel filter was subtracted from the original image to remove deterministic background uniformities, as detailed in section 2.1. The relative spatial resolution of the detectors was

assessed in the two projections based on a previously published technique (Seco *et al* 2013). Three profiles were taken in the right lateral projection starting in spine and ending in lung as indicated in figure 7. Three profiles in the radial direction were taken on the AP projection in the upper left corner, spanning the boundary between chest wall and lung. A sigmoid curve was fit to the data, with all fits having an R^2 greater than 0.99, and the differential was calculated to produce a Gaussian. The full width half maximum (FWHM) of the Gaussian was measured.

2.3. Clinical images
Clinical images were collected with institutional review board approval (DFCI#18-517). Analyzing the performance of the imager in actual clinical scenarios (which include inter-individual differences in anatomy and motion) is a critical step in translating the prototype to every-day use. Therefore, we assessed imager performance for fiducial, bony, and soft tissue differentiation in a cohort of 12 patients.

The MLI was mounted onto the TrueBeam's MV imager arm and connected to the standard optical data cable. A computer with a frame grabber card was connected to an output jack of the TrueBeam's XI cabinet. Five stereotactic body radiotherapy (SBRT) spine patients and seven SBRT liver patients made up the initial clinical cohort. Their plans were generated routinely, and without consideration for the imaging study. The MLI panel was placed at 180 cm SID during the delivery of the VMAT treatment fields to ensure adequate patient clearance, and the frame grabber card passively acquired images at an average of 10.1 frames per seconds. Two fractions of each patient were imaged in this fashion: one fraction with the MLI in 4-layer mode and one fraction with the MLI in 1-layer mode. Paired frames from the two fractions were evaluated for CNR and SNR. A 5×5 median pixel filter was subtracted from the original images to remove deterministic background uniformities, as detailed in section 2.1. For the spine analysis, the bone was used as signal and soft tissue as background. For the liver analysis, two different ratios were determined: the dome of the liver as signal and the lung superior to the liver as background, and a fiducial as signal and the surrounding tissue as background.

3. Results

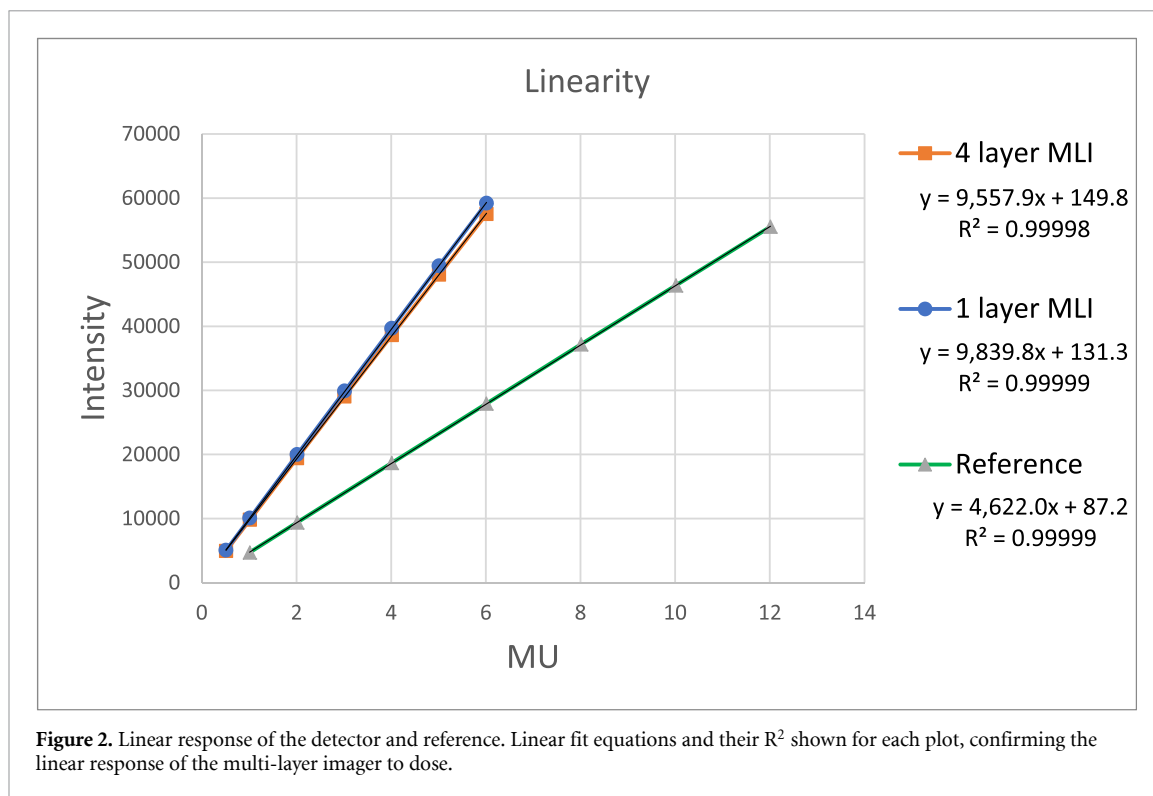### 3.1. MLI detector characterization
The MLI detector response to imaging dose demonstrated strong linearity with the linear fit $R^2 > 0.9999$. (figure 2). The thicker scintillator on the MLI could explain the more rapid saturation in comparison to the reference detector. The response of each of the four MLI layers is averaged rather than added, explaining why the 4-layer and 1-layer responses are nearly identical.

Las Vegas phantom images for each detector configuration are shown in figures 3(a)–(c). Qualitatively, one can see better visibility and smoothness in the 4-layer MLI image. Quantitatively, the 4-layer MLI CNR has an enhancement ratio of 3.02 relative to the reference detector, and 1.79 relative to the 1-layer acquisition with the MLI. The SNR also shows a ratio of 3.02 for the 4-layer versus reference detector, and 1.99 versus the 1-layer acquisition with the MLI.

MTF calculation (figure 4) demonstrates best resolution for the reference detector, likely due to the thinner scintillator. The 4-layer configuration has somewhat lower MTF than the single (top MLI) layer in the mid-frequency range, likely due to increased scatter in the MLI for lower layers (Hu *et al* 2018a). The NPS measurements show a major reduction in the noise for the thicker scintillator configurations, with 4-layer mode presenting an 82.5% decrease in qNNPS compared to reference at zero frequency (figure 5). DQE, calculated from the measured MTF and qNNPS, shows higher values for the MLI configurations, driven mainly by the noise reduction (figure 6). DQE(0) for the reference detector (calculated as described in section 2.1) was 1.7%, 1-layer MLI 2.6%, and 4-layer MLI 9.7%, a 5.7 fold increase over reference.

3.2. Phantom study
Quantitative evaluation of the CNR and SNR in the thorax phantom followed a similar trend (figure 7). The ratio of 4-layer:1-layer CNR is 1.80 and SNR is 1.92. 4-layer:reference CNR is 3.18 and SNR is 3.38. The FWHM of the differential of the transverse profile from spine to bone is 2.58 mm for 4-layer, 2.01 mm for 1-layer, and 1.99 mm for reference detector. The radial profile from chest wall to lung is 3.14 mm for 4-layer, 2.48 mm for 1-layer, and 2.45 mm for the reference detector, indicating decreased spatial resolution for the 4-layer MLI acquisition. These profile results are consistent with the MTF results in section 3.1, where increased scatter for the lower MLI layers may degrade spatial resolution. Geometric concerns for using multiple layers are unlikely to be notable. The distance between layer 1 and layer 4 is 9.6 mm. If layer 1 is 1500 mm from the source, in a worst-case scenario where the field edge lands right at the edge of the detector, 215 mm from the center, divergence will lead to a 1.36 mm or about 4 pixel difference in layer 4.

Figure 2. Linear response of the detector and reference. Linear fit equations and their R^2 shown for each plot, confirming the linear response of the multi-layer imager to dose.

3.3. Clinical images

Images were successfully acquired during clinical treatment delivery for all 12 patients. Other than the several seconds necessary for extending the EPID, the patient's treatment time was unaffected by the experiments. Image acquisition for the first patient was impacted by 122 dropped frames due to hard disk drive write speeds. After replacing the hard drive with a solid state drive (SSD), dropped frames ceased to be an issue.
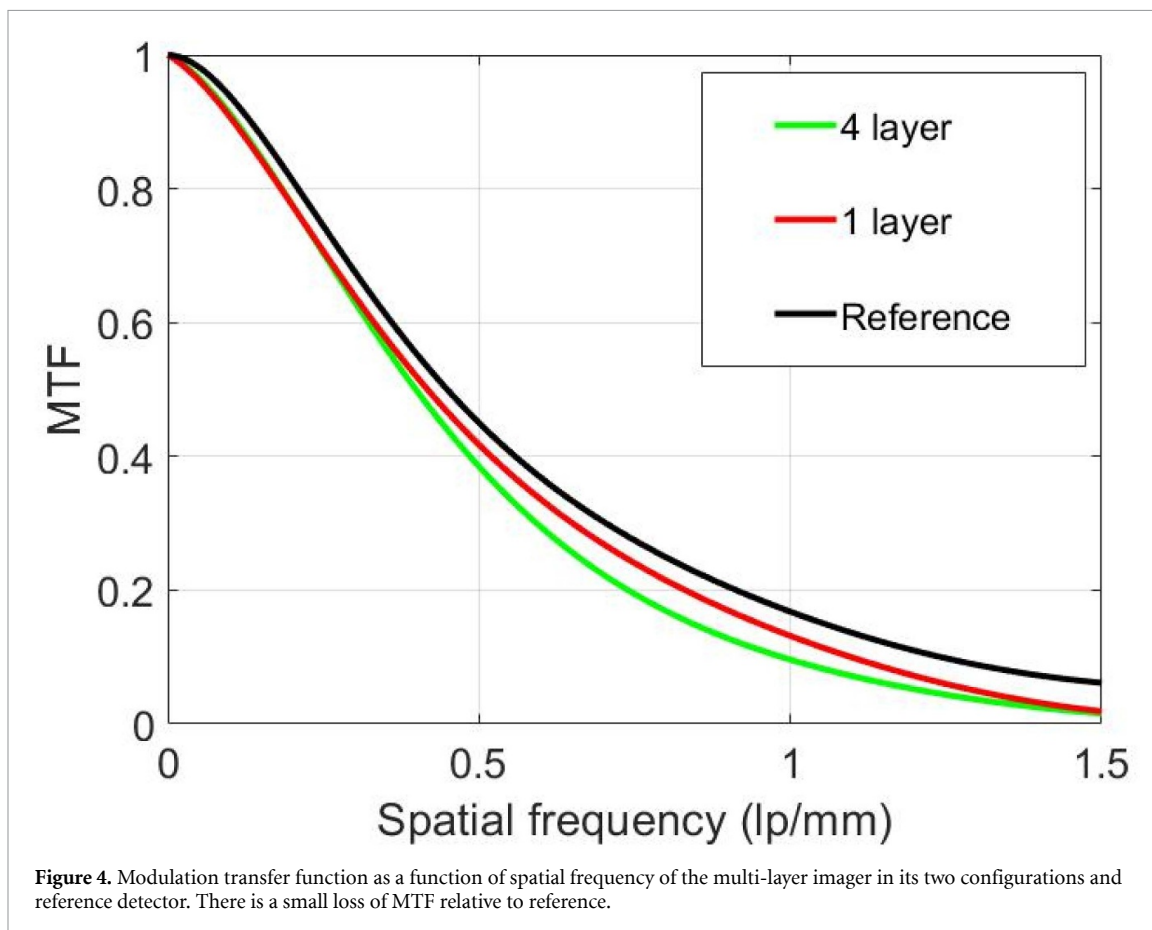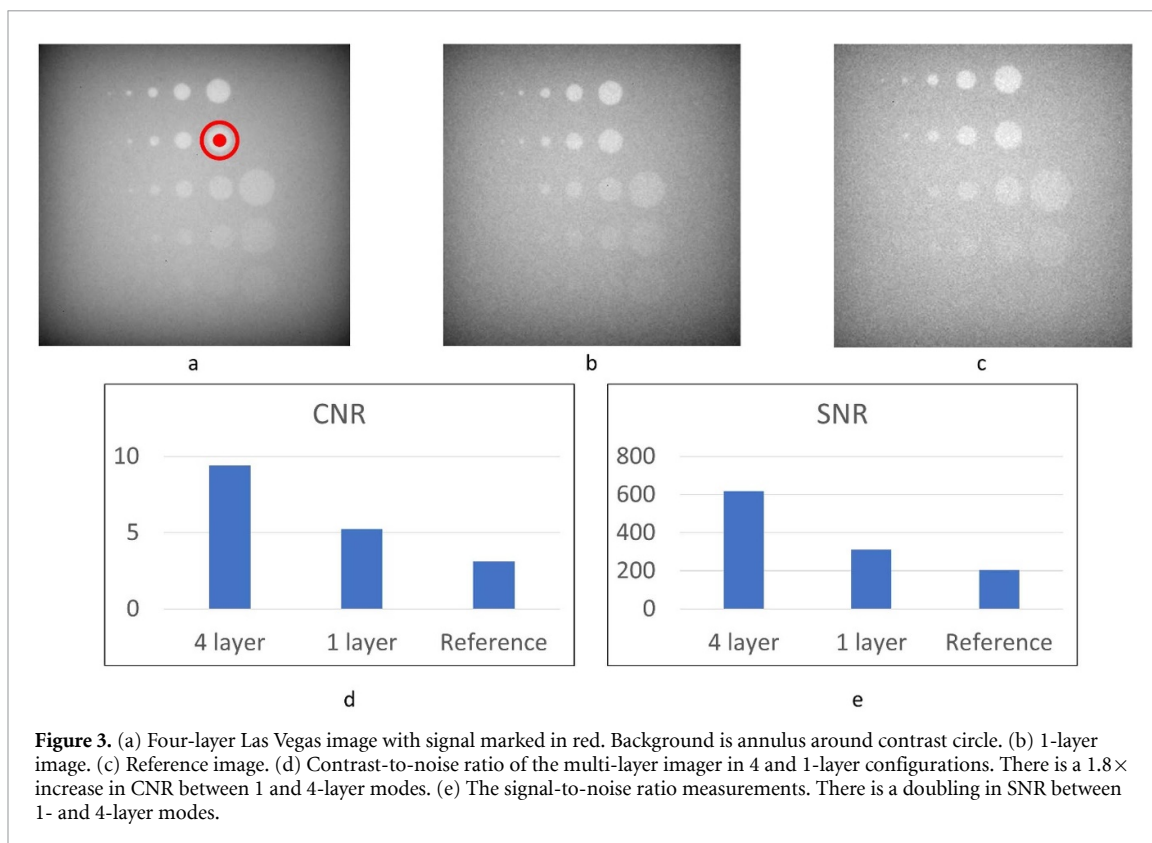
For the 5 spine patients, all had 2–3 VMAT arcs and per fraction doses ranging from 600 cGy to 700 cGy. On average over 500 frames per arc were collected, though some were ill-suited for our analysis due to MLC modulation. For the 7 liver patients, all had 2–3 VMAT arcs and per fraction doses ranging from 900 cGy to 1200 cGy. Due to respiratory safety gating, each arc often resulted in over 1000 collected frames, as the imager kept acquiring during beam off. MLC modulation also made some frames challenging to analyze.
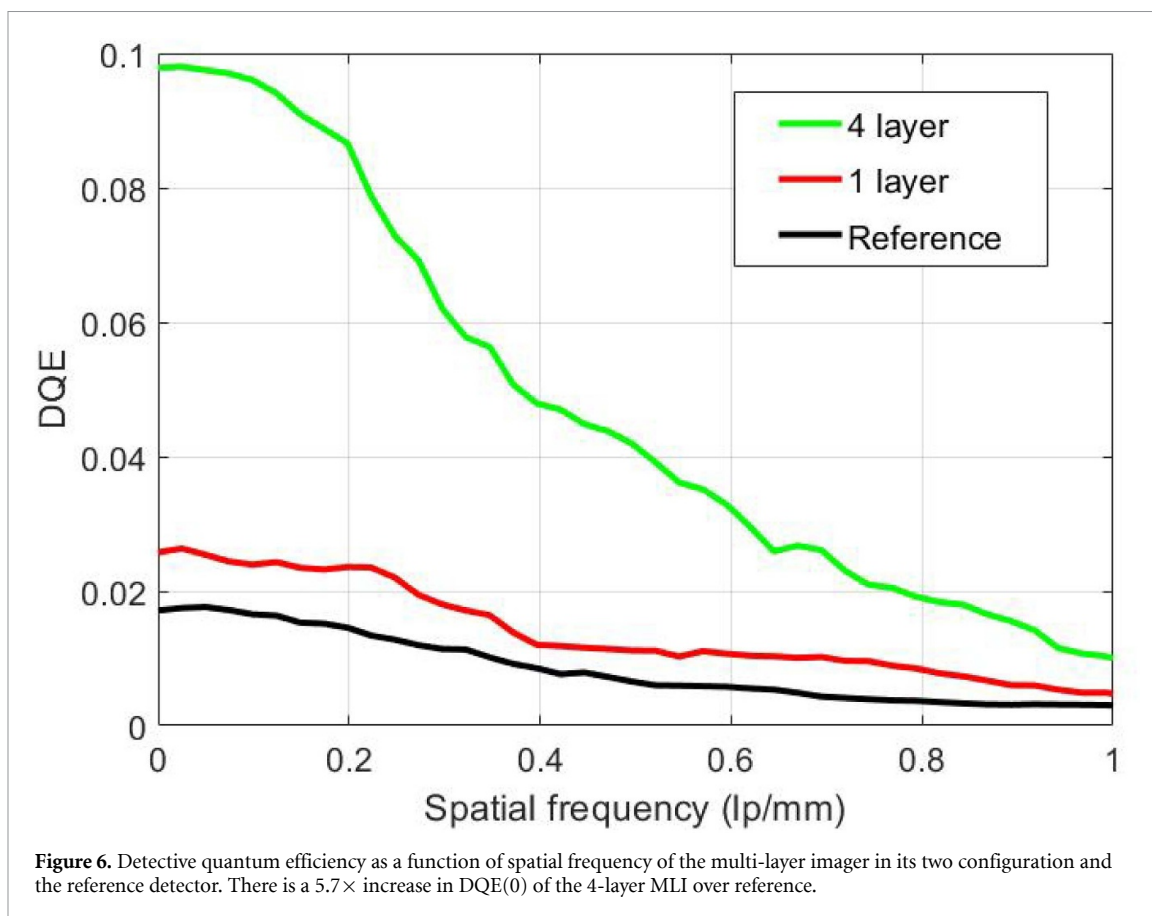
The spine patient images were evaluated for CNR and SNR for frames in which the spine was visible (figure 8). The 4-layer:1-layer ratio of CNR is 1.52 and SNR is 2.03. This result is similar to values measured on a Las Vegas phantom and a thorax phantom, showing that the detector's performance is consistent in a clinical scenario with bone and soft tissue.

Representative 4-layer and 1-layer matching liver treatment field frames are shown in figures 9(a)–(b). The fiducial is circled and magnified in an inset to aid in visualization. Forty different paired frames from the seven different patient data sets were analyzed, and the average value $+/-$ one standard deviation were calculated. The CNR 4-layer:1-layer for the liver dome is 1.88 $+/-$ 0.04 and the SNR is 1.96 $+/-$ 0.03. The same calculations for the liver fiducial are CNR of 1.87 $+/-$ 0.05 and SNR of 1.92 $+/-$ 0.06 (figure 10). These results are consistent with characterization and pre-clinical measurements, showing that the detector's performance for soft tissue and fiducial delineation carry over to patient imaging. By averaging the results from multiple sets of paired frames, any partial frame effects caused by acquiring in asynchronous mode may be minimized.

4. Discussion

A prototype EPID with four detection layers was characterized and deployed for in-treatment patient imaging. The 4-layer MLI performance was compared to the Varian AS-1200 and to the top layer only of the prototype MLI itself. The increased DQE of the 4-layer MLI configuration is attributable to both a thicker scintillator in each layer and the stacking of multiple detectors. The thicker scintillator improved quantum efficiency but also increased optical spread, reducing MTF. Previous work has shown that noise reduction is more important than spatial resolution for radiotherapy imaging applications (Hu *et al* 2017). In clinical images, improvements in CNR and SNR largely followed expectations from theory and from the experimental phantom data.

Figure 3. (a) Four-layer Las Vegas image with signal marked in red. Background is annulus around contrast circle. (b) 1-layer image. (c) Reference image. (d) Contrast-to-noise ratio of the multi-layer imager in 4 and 1-layer configurations. There is a 1.8× increase in CNR between 1 and 4-layer modes. (e) The signal-to-noise ratio measurements. There is a doubling in SNR between 1- and 4-layer modes.

Figure 4. Modulation transfer function as a function of spatial frequency of the multi-layer imager in its two configurations and reference detector. There is a small loss of MTF relative to reference.

Figure 5. Normalized noise power spectrum as a function of spatial frequency of the multi-layer imager in its two configurations and reference detector. Noise performance is superior with the 4-layer MLI.

Figure 6. Detective quantum efficiency as a function of spatial frequency of the multi-layer imager in its two configuration and the reference detector. There is a 5.7× increase in DQE(0) of the 4-layer MLI over reference.

Figure 7. (a) AP image of embedded tumor in thorax phantom on the 4-layer MLI, signal in tumor and background ROIs circled. Red lines mark where the radial profiles were taken. (b) Right lateral image of the thorax phantom on the 4-layer MLI. Red lines mark where the profiles were taken. (c) Measured contrast-to-noise ratio of the multi-layer imager in its two configurations and the reference detector. There is a 1.8× increase of CNR between the 1-layer and 4-layer MLI. (d) Signal-to-noise ratio of the same group of detectors. There is a 1.9× increase of SNR between 1-layer and 4-layer MLI. (e) Example of a sigmoidal fit for a profile across the bone/lung interface in figure (b). The X position is given in pixel units with each pixel being 0.336 mm across.

Figure 8. (a) Captured frame from a spine treatment in 4-layer mode. Areas used for signal and background marked. (b) Matching frame from 1-layer mode, with signal and background areas marked. (c) Measured contrast-to-noise ratio for the multi-layer imager in its two configurations. There is a 1.5× increase in CNR from 1-layer to 4-layer MLI. (d) Measured signal-to-noise ratio for the MLI in its two configurations. There is a 2.0× increase in SNR from 1-layer to 4-layer MLI.

The prototype was constructed with standard GOS scintillators but is intended to be a platform that, with minimal mechanical changes, can accommodate layers of differing materials and thicknesses. Our group is working to determine useful compositions of different scintillator materials in the separate layers (Hu *et al* 2018a) as well as finding optimal weighting for the contribution of each layer (Valencia Lozano *et al* 2020) The prototype evaluated in this study can be used in future clinical translation efforts for MLI configurations deemed to be promising.
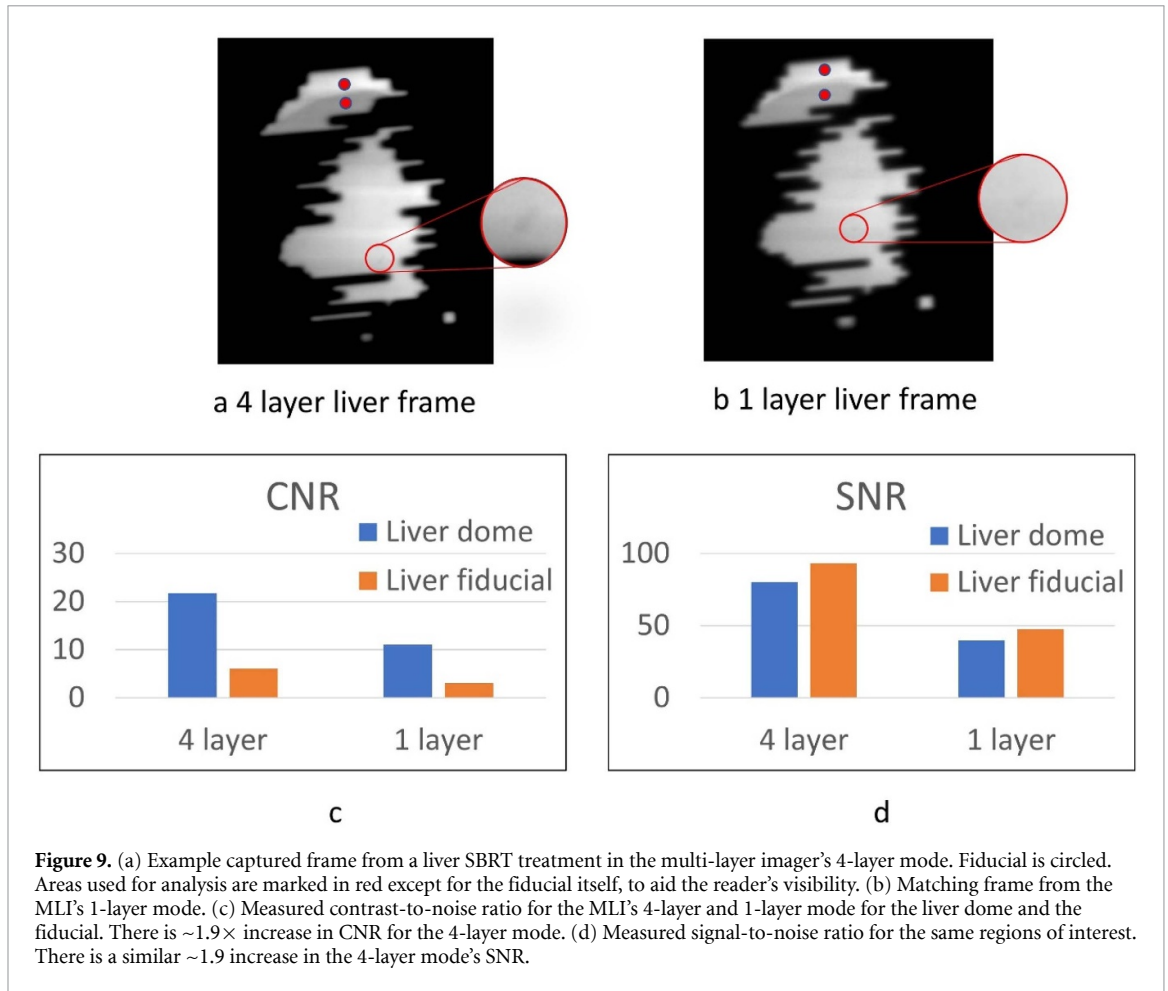
Figure 9. (a) Example captured frame from a liver SBRT treatment in the multi-layer imager's 4-layer mode. Fiducial is circled. Areas used for analysis are marked in red except for the fiducial itself, to aid the reader's visibility. (b) Matching frame from the MLI's 1-layer mode. (c) Measured contrast-to-noise ratio for the MLI's 4-layer and 1-layer mode for the liver dome and the fiducial. There is ~1.9× increase in CNR for the 4-layer mode. (d) Measured signal-to-noise ratio for the same regions of interest. There is a similar ~1.9 increase in the 4-layer mode's SNR.
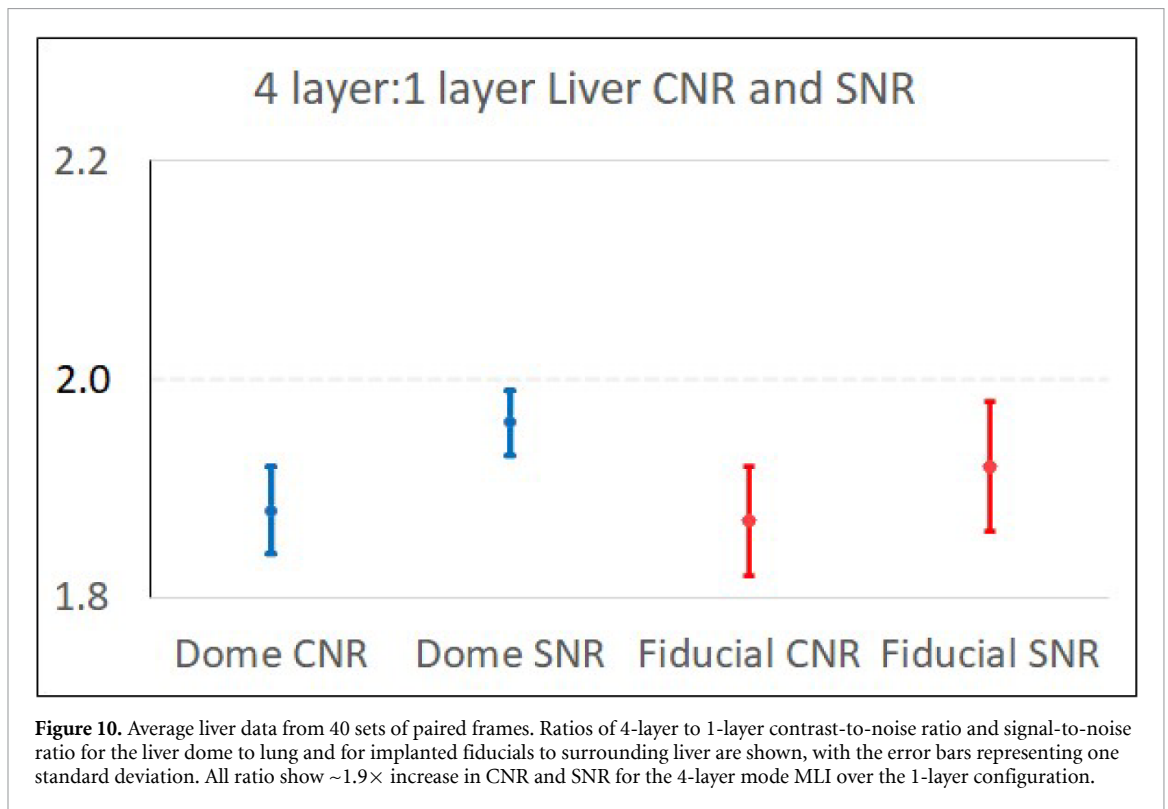

Figure 10. Average liver data from 40 sets of paired frames. Ratios of 4-layer to 1-layer contrast-to-noise ratio and signal-to-noise ratio for the liver dome to lung and for implanted fiducials to surrounding liver are shown, with the error bars representing one standard deviation. All ratio show ~1.9× increase in CNR and SNR for the 4-layer mode MLI over the 1-layer configuration.

An MV detector with better DQE and CNR performance will improve several clinical imaging applications. Megavoltage cone-beam computed tomography (MV-CBCT) could be performed at lower

doses or with improved performance at the same dose (Myronakis *et al* 2020). A recent study demonstrated the viability of MV-CBCT as the planning image set for urgent radiotherapy cases (Held *et al* 2015). Patient position verification in the presence of high atomic number (Z) objects, such as orthopedic hardware surrounding paraspinous tumors, hip prostheses, and dental implants would likely be superior with MV-CBCT rather than traditional kilovoltage cone-beam computed tomography (kV-CBCT) (Wu *et al* 2014). Furthermore, a recent investigation of combined kV/MV-CBCT imaging for shorter scan times and metal artifact reduction demonstrated that a higher DQE MV detector would be useful for this new technique (Lindsay *et al* 2019).

Numerous reports (Keall *et al* 2006, Yoganathan *et al* 2017) have reviewed some possible methods to minimize the impact of respiration-induced tumor motion. In this context, EPID-based tumor tracking solutions has two significant advantages: 1. Tracking is not dependent upon external surrogates with possibly variable correlation to internal anatomy (Ionascu *et al* 2007). 2. The treatment field itself supplies the radiation, adding no extra dose for imaging. Our prototype MLI may have utility in detecting the boundary between lung tumor and lung, or between fiducial and its surrounding tissue, making real-time tracking more feasible. This hypothesis is currently the subject of a parallel study.

5. Conclusion

In this study, we characterized the performance of a prototype MV MLI, conducted pre-clinical testing on an anthropomorphic phantom, and analyzed preliminary data from 12 patients' treatments. The stacking of multiple, thicker detector layers in the MLI results in large improvements in DQE and CNR for pre-clinical and clinical measurements.

Acknowledgments

References

Antonuk L, Yorkston J, Boudry J, Longo M, Jimenez J and Street R 1990 Development of hydrogenated amorphous silicon sensors for high energy photon radiotherapy imaging *IEEE Trans. Nucl. Sci.* **37** 165–70

Antonuk L E 2002 Electronic portal imaging devices: a review and historical perspective of contemporary technologies and research *Phys. Med. Biol.* **47** R31–R65

Bakhtiari M, Kumaraswamy L, Bailey D W, de Boer S, Malhotra H K and Podgorsak M B 2011 Using an EPID for patient-specific VMAT quality assurance *Med. Phys.* **38** 1366–73

Celi S, Costa E, Wessels C, Mazal A, Fourquet A and Francois P 2016 EPID based *in vivo* dosimetry system: clinical experience and results *J. Appl. Clin. Med. Phys.* **17** 262–76

El-Mohri Y, Jee K W, Antonuk L E, Maolinbay M and Zhao Q 2001 Determination of the detective quantum efficiency of a prototype, megavoltage indirect detection, active matrix flat-panel imager *Med. Phys.* **28** 2538–50

Ferguson D *et al* 2020 Automated MV markerless tumor tracking for VMAT *Phys. Med. Biol.* **65** 125011

Fuangrod T, Woodruff H C, Rowshanfarzad P, O'Connor D J, Middleton R H and Greer P B 2014 An independent system for real-time dynamic multileaf collimation trajectory verification using EPID *Phys. Med. Biol.* **59** 61–81

Fujita H, Tsai D Y, Itoh T, Doi K, Morishita J, Ueda K and Ohtsuka A 1992 A simple method for determining the modulation transfer function in digital radiography *IEEE Trans. Med. Imaging* **11** 34–39

Held M, Sneed P K, Fogh S E, Pouliot J and Morin O 2015 Feasibility of MV CBCT-based treatment planning for urgent radiation therapy: dosimetric accuracy of MV CBCT-based dose calculations *J. Appl. Clin. Med. Phys.* **16** 458–71

Herman M G, Balter J M, Jaffray D A, Mcgee K P, Munro P, Shalev S, Van Herk M and Wong J W 2001 Clinical use of electronic portal imaging: report of AAPM radiation therapy committee task group 58 *Med. Phys.* **28** 712–37

Hu Y H *et al* 2018a Physics consideration in MV-CBCT multi-layer imaging design *Phys. Med. Biol.* **63** 125016

Hu Y H *et al* 2018b Feasibility of closed-MLC tracking using high sensitivity and multi-layer electronic portal imagers *Phys. Med. Biol.* **63** 235030

Hu Y H, Myronakis M, Rottmann J, Wang A, Morf D, Shedlock D, Baturin P, Star-Lack J and Berbeco R 2017 A novel method for quantification of beam's-eye-view tumor tracking performance *Med. Phys.* **44** 5650–9

Hu Y H *et al* 2019 Characterizing a novel scintillating glass for application to megavoltage cone-beam computed tomography *Med. Phys.* **46** 1323–30

International Electrotechnical Commission 2003 Medical electrical equipment—characteristics of digital x-ray imaging devices—part 1: determination of the detective quantum efficiency, IEC-62220-1

Ionascu D, Jiang S B, Nishioka S, Shirato H and Berbeco R I 2007 Internal-external correlation investigations of respiratory induced motion of lung tumors *Med. Phys.* **34** 3893–903

Jensen C, Urribarri J, Cail D, Rottmann J, Mishra P, Lingos T, Niedermayr T and Berbeco R 2014 Cine EPID evaluation of two non-commercial techniques for DIBH *Med. Phys.* **41** 021730

Keall P J *et al* 2006 The management of respiratory motion in radiation oncology report of AAPM task group 76 *Med. Phys.* **33** 3874–900

Lindsay C, Bazalova-Carter M, Wang A, Shedlock D, Wu M, Newson M, Xing L, Ansbacher W, Fahrig R and Star-Lack J 2019 Investigation of combined kV/MV CBCT imaging with a high-DQE MV detector *Med. Phys.* **46** 563–75

Munro P and Bouius D C 1998 X-ray quantum limited portal imaging using amorphous silicon flat-panel arrays *Med. Phys.* **25** 689–702

Myronakis M, Fueglistaller R, Rottmann J, Hu Y H, Wang A, Baturin P, Huber P, Morf D, Star-Lack J and Berbeco R 2017 Spectral imaging using clinical megavoltage beams and a novel multi-layer imager *Phys. Med. Biol.* **62** 9127–39

Myronakis M *et al* 2020 Low-dose megavoltage cone-beam computed tomography using a novel multi-layer imager (MLI) *Med. Phys.* accepted 2020 Apr;47(4):1827-1835

Nijsten S M, Mijnheer B J, Dekker A L, Lambin P and Minken A W 2007 Routine individualised patient dosimetry using electronic portal imaging devices *Radiother. Oncol.* **83** 65–75

Partridge M, Ebert M and Hesse B M 2002 IMRT verification by three-dimensional dose reconstruction from portal beam measurement *Med. Phys.* **29** 1847–58

Rottmann J, Keall P and Berbeco R 2013a Markerless EPID image guided dynamic multi-leaf collimator tracking for lung tumors *Phys. Med. Biol.* **58** 4195–204

Rottmann J, Keall P and Berbeco R 2013b Real-time soft tissue motion estimation for lung tumors during radiotherapy delivery *Med. Phys.* **40** 091713

Rottmann J, Morf D, Fueglistaller R, Zentai G, Star-Lack J and Berbeco R 2016 A novel EPID design for enhanced contrast and detective quantum efficiency *Phys. Med. Biol.* **61** 6297–306

Seco J, Oumano M, Depauw N, Dias M F, Teixeira R P and Spadea M F 2013 Characterizing the modulation transfer function (MTF) of proton/carbon radiography using Monte Carlo simulations *Med. Phys.* **40** 091717

Star-Lack J *et al* 2015 A piecewise-focused high DQE detector for MV imaging *Med. Phys.* **42** 5084–99

Star-Lack J, Sun M, Meyer A, Morf D, Constantin D, Fahrig R and Abel E 2014 Rapid Monte Carlo simulation of detector DQE(f) *Med. Phys.* **41** 031916

Street R, Nelson S, Antonuk L and Perez Mendez V 1990 Amorphous silicon sensor arrays for radiation imaging *MRS Proc. vol 192* (Cambridge University Press) p 441

Swank R K 1973 Absorption and noise in x-ray phosphors *J. Phys. D: Appl. Phys.* **44** 4199–203

Ueda Y, Miyazaki M, Nishiyama K, Suzuki O, Tsujii K and Miyagi K 2012 Craniocaudal safety margin calculation based on interfractional changes in tumor motion in lung SBRT assessed with an EPID in cine mode *Int. J. Radiat. Oncol.* **83** 1064–9

Valencia Lozano I *et al* 2020 Evaluation of an image-based weighting approach for megavoltage multilayer imagers *WE-B-TRACK 2-6, AAPM/COMP annual meeting Vancouver, Canada*

Warkentin B, Steciw S, Rathee S and Fallone B G 2003 Dosimetric IMRT verification with a flat-panel EPID *Med. Phys.* **30** 3143–55

Wendling M, Mcdermott L N, Mans A, Sonke J J, van Herk M and Mijnheer B J 2009 A simple backprojection algorithm for 3D in vivo EPID dosimetry of IMRT treatments *Med. Phys.* **36** 3310–21

Woodruff H C, Fuangrod T, Rowshanfarzad P, Mccurdy B M and Greer P B 2013 Gantry-angle resolved VMAT pretreatment verification using EPID image prediction *Med. Phys.* **40** 081715

Wu M, Keil A, Constantin D, Star-Lack J, Zhu L and Fahrig R 2014 Metal artifact correction for x-ray computed tomography using kV and selective MV imaging *Med. Phys.* **41** 121910

Yip S S F, Rottmann J, Chen H, Morf D, Fueslistaller R, Star-Lack J, Zentai G and Berbeco R 2017 Technical note: combination of multiple EPID imager layers improves image quality and tracking performance of low contrast-to-noise objects *Med. Phys.* **44** 4847–53

Yoganathan S A, Maria Das K J, Agarwal A and Kumar S 2017 Magnitude, impact, and management of respiration-induced target motion in radiotherapy treatment: a comprehensive review *J. Med. Phys.* **42** 101–15

Zhao W, Ristic G and Rowlands J A 2004 X-ray imaging performance of structured cesium iodide scintillators *Med. Phys.* **31** 2594–605

2.3 Improvements in beam's eye view fiducial tracking using a novel multilayer imager

This paper presents the results of a clinical trial comparing the performance of the MLI versus that of a single layer EPID in real-world clinical applications.   A modified tracking algorithm based on the work in chapter 2.1 was utilized.   Six patients with gold fiducials placed near liver metastases were imaged during their treatments, once with the MLI and once with a single layer imager. Tracking accuracy and efficiency was found to be significantly improved with the MLI, demonstrating that a multilayer architecture has the potential to improve clinical applications like beam's-eye-view tumor tracking.

Further analyses were undertaken in order to explain the source of the improved performance.   We discovered a positive correlation between the noise reduction afforded by the multiple layers and increased tracking execution. This finding offers a potential tactic for improving future EPID applications.

The thesis author designed the study with counsel from his co-authors.   He was personally present at every patient's treatment to manage the data acquisition.   He analyzed the gathered data and prepared the associated manuscript.

Physics in Medicine & Biology

IPEM Institute of Physics and Engineering in Medicine

PAPER

Improvements in beam's eye view fiducial tracking using a novel multilayer imager

T C Harris[1,2,3] ⓘ, J Seco[2,3], D Ferguson[4], M Jacobson[1], M Myronakis[1], I Valencia Lozano[1] ⓘ, M Lehmann[5], P Huber[5], R Fueglistaller[5], D Morf[5], H J Mamon[1], J D Mancias[1], N E Martin[1] and R I Berbeco[1]

[1] Department of Radiation Oncology, Brigham and Women's Hospital, Dana Farber Cancer Institute and Harvard Medical School, Boston, MA, United States of America
[2] BioMedical Physics in Radiation Oncology, DKFZ, Heidelberg, Germany
[3] Department of Physics, University of Heidelberg, Heidelberg, Germany
[4] Department of Radiation Oncology, University of California San Francisco, San Francisco, CA, United States of America
[5] Varian Medical Systems, Baden-Dattwil, Switzerland

E-mail: tharris@bwh.harvard.edu

Abstract

Purpose. Electronic portal image devices (EPIDs) have been investigated previously for beams-eye view (BEV) applications such as tumor tracking but are limited by low contrast-to-noise ratio and detective quantum efficiency. A novel multilayer imager (MLI), consisting of four stacked flat-panels was used to measure improvements in fiducial tracking during liver stereotactic body radiation therapy (SBRT) procedures compared to a single layer EPID. *Methods.* The prototype MLI was installed on a clinical TrueBeam linac in place of the conventional DMI single-layer EPID. The panel was extended during volumetric modulated arc therapy SBRT treatments in order to passively acquire data during therapy. Images were acquired for six patients receiving SBRT to liver metastases over two fractions each, one with the MLI using all 4 layers and one with the MLI using the top layer only, representing a standard EPID. The acquired frames were processed by a previously published tracking algorithm modified to identify implanted radiopaque fiducials. Truth data was determined using respiratory traces combined with partial manual tracking. Results for 4- and 1-layer mode were compared against truth data for tracking accuracy and efficiency. Tracking and noise improvements as a function of gantry angle were determined. *Results.* Tracking efficiency with 4-layers improved to 82.8% versus 58.4% for the 1-layer mode, a relative improvement of 41.7%. Fiducial tracking with 1-layer returned a root mean square error (RMSE) of 2.1 mm compared to 4-layer RMSE of 1.5 mm, a statistically significant ($p < 0.001$) improvement of 0.6 mm. The reduction in noise correlated with an increase in successfully tracked frames ($r = 0.913$) and with increased tracking accuracy (0.927). *Conclusion.* Increases in MV photon detection efficiency by utilization of a MLI results in improved fiducial tracking for liver SBRT treatments. Future clinical applications utilizing BEV imaging may be enhanced by including similar noise reduction strategies.

1. Introduction

Electronic portal imaging devices (EPIDs) are available on most linear accelerators, replacing film cassettes for acquiring MV portal images for radiotherapy localization and verification (Herman *et al* 2001). Over time, a number of additional clinical applications for MV imaging have been developed. Of particular interest is the *cine* mode, in which the EPID acquires sequential images of the treatment field after it has exited the patient.

MV cine imaging, also sometimes referred to as 'beam's-eye-view' (BEV) imaging, offers several advantages in comparison to on-board orthogonal kV imaging. Importantly, the patient receives no additional imaging dose; for real-time applications, continuous kV fluoroscopy dose may become substantial (Murphy *et al* 2007). MV cine images also show the actual anatomy undergoing irradiation in real-time, rather than an orthogonal

view. Each individual MV cine frame is two-dimensional, which can be sufficient since the third dimension, depth, is dosimetrically not as significant for high energy x-ray irradiation. Despite these benefits, clinical implementation of EPIDs to manage patient motion has been hindered by the inherently low contrast of MV imaging and the relatively low detective quantum efficiency (DQE) of currently used EPIDs (Antonuk 2002).

Advanced real-time applications enabled by MV *cine* imaging include treatment verification and monitoring. BEV automated tracking of implanted fiducials (Keall *et al* 2004, Park *et al* 2009) during beam delivery helps ensure accurate dose delivery while potentially enabling a more conformal treatment. However, dynamic modulation of the treatment aperture and direction complicate the task of tracking fiducial locations. Some researchers have directly addressed the issue of MLCs obscuring fiducials (Azcona *et al* 2013, Yue *et al* 2011, Hu *et al* 2018). Others have developed indirect methods such as using combined imaging modalities with kV (Wiersma *et al* 2008, Cho *et al* 2011), modifying the MLCs during treatment planning to optimize fiducial visibility (Happersett *et al* 2019), and determining best fiducial placement to maximize frames containing a fiducial (Ma *et al* 2018).

There has been extensive research dedicated to improving EPID performance. Some investigations have focused on novel scintillator materials (Hu *et al* 2019) and scintillator construction, such as structured phosphors (Zhao *et al* 2004) and pixelated scintillators (Star-Lack *et al* 2015). Stacking several layers of current generation components is an economical and relatively practical approach. This strategy boosts photon collection efficiency without an increase in Swank noise (Swank 1973). Using multiple detection layers provides a substantial elevation in DQE while preserving field of view and spatial resolution (Harris 2020).

Characterization of the MV imaging panel used to acquire data for the present study has been previously published (Harris *et al* 2020). Here, we extend our prior work by studying the impact of this novel multi-layer EPID on fiducial tracking in BEV images acquired during clinical SBRT procedures. Previously, we demonstrated a 1.87 fold increase in the contrast-to-noise ratio of a fiducial to surrounding liver tissue when using a 4-layer EPID compared to 1-layer. The objective of the present study was to study how this enhanced performance translates to the clinical application of fiducial tracking, in terms of both fiducial tracking accuracy and efficiency, in the presence of unfavorable anatomic arrangements or treatment beam apertures.

2. Materials and method

2.1. Multi-layer imager (MLI)

We used a novel MLI comprised of four identical layers of: (1) a copper sheet to convert photons to secondary electrons, and shield against low energy scattered radiation. (2) Terbium-doped gadolinium oxysulfide (GOS) as a scintillator to convert radiation to optical photons. (3) Hydrogen doped amorphous silicon deposited on a glass substrate to form a pixelated array of photodiode thin film transistors to detect the optical photons. This flat-panel imager's composition is similar to current commercially available EPIDs, although the MLI's scintillator has a thickness of 0.436 mm (200 mg cm^{-2}) per layer. This thickness matches what is available on Varian's Halcyon clinical treatment platform but is thicker than the AS-1200 scintillator (0.290 mm, 113 mg cm^{-2}) available on most other Varian linacs.

The MLI's firmware permits it to run in 4-layer mode—in which the response of each layer is averaged together—or in 1-layer mode utilizing just the top layer, thus approximating a standard EPID. In our previously published work, the DQE(0) for 6 MV was found to be 1.7% for the AS-1200, 2.6% for the MLI 1-layer mode, and 9.7% for the MLI 4-layer mode, a $5.7\times$ increase in performance over the standard commercially available model. Both 4-layer and 1-layer acquisition modes were used in this study to compare the performance difference of a MLI to a standard single-layer EPID.

2.2. Data acquisition

Clinical images were collected under Dana-Farber Cancer Institute IRB approval (DFCI#18-517). The MLI was placed inside the standard AS-1200 housing and collision frame, mounted onto a TrueBeam's MV imager arm, and connected to the standard optical data cable. A computer with a frame grabber card was connected to an output jack of the TrueBeam's XI node to collect the stream of image frames.

BEV images during SBRT were passively acquired for six patients with liver metastases (four with one metastasis; two with two metastases). Five of the six patients had tumors in the right lobe, while the sixth patient had one lesion in the right lobe and one in the left lobe. Patients received 5 fraction SBRT using 2–3 VMAT arcs delivering per fraction doses ranging from 900 to 1200 cGy. Beam energy was 6 MV in flattening-filter-free (FFF) mode, with the beam calibrated to deliver 1 cGy M^{-1} U^{-1} at d_{max} with a 10 cm $\times$ 10 cm open field, 100 cm SAD. Patients received both a standard helical planning CT and a 4D CT using Varian's RGSC gating system. Treatment plans were generated routinely, and without consideration for the imaging study. The MLI was extended to 180 cm source to imager distance (SID) to ensure adequate patient clearance. Acquired images were

flood field, dark field, and pixel defect map corrected. On average, 10.1 frames per second were passively gathered during patients' beam deliveries.

Patients had three gold cylindrical fiducials (diameter 0.8 mm, length 3 mm, Fiduciary Marker Kit, Best Medical International) implanted in their PTVs, except for two of the patients who had two separate lesions. Those two patients had two fiducials implanted in each of their two PTVs, for a total of four implanted markers each. Fiducials were later calculated to have an average spacing of 3.3 cm $+/-$ 1.4 cm. Patients received an initial setup CBCT and triggered kV images every 5 degrees of rotation to continue verifying positioning, as is our standard of care. Using RGSC, 4 of the patients were monitored by 'safety gating' and 2 of the patients were treated using light inspiration breath hold.

BEV images were acquired for each patient across two treatment fractions, each consisting of 2–3 treatment arcs. Full 360 degree arcs could not be delivered because the treatment isocenters were located in the liver and thus too lateral in the patient to avoid collisions. Therefore, gantry arcs started at 181 degrees and terminated from 320 to 30 degrees, after which the couch was temporarily shifted laterally to allow the gantry to pass without patient collision, followed by treatment from the contralateral side. One fraction was performed with the MLI in 4-layer acquisition mode, and the other fraction with the MLI in 1-layer acquisition mode. The treatment delivery procedure was not altered to accommodate the imaging study other than the several seconds needed to extend the MV panel at the start of the treatment fraction.

2.3. Tracking algorithm

The fiducial tracking algorithm used in this study is a modification of previously published work from our group, initially designed for marker-less tracking (Ferguson *et al* 2020) and will be briefly summarized here.

The tracking algorithm automatically detects features of interest in 2D image frames and tracks those features while visible within the aperture. Each image frame is initially masked by the collimator jaw settings and the MLC positions, as well as a region around them to exclude any gradient near a boundary. After masking, candidate features for tracking are described by a cluster of templates generated along lines of high local variance. The cluster of templates helps to encode the shape of the feature. Template matching is performed on subsequent images using the calculated normalized cross-correlation (NCC) on the variance map. Templates are scored by a weighted combination of multiple factors: the NCC value of the template, divergence from the original relative template orientations, and the average stability of the templates (how often they contribute to successful feature tracking).

Although the algorithm was initially designed for tracking tumors in lung directly, radiopaque fiducials create an area of high local variance on the images and thus should be identified easily. In addition, we made modifications to the code to optimize it for fiducial tracking. The contour created by the templates was evaluated for shape and spatial dimensions, identifying if the feature was shaped like a fiducial—either circular 'head-on,' cylindrical from the side, or some eccentric angle between the two. The tracker was also provided with the isocenter and fiducial coordinates from the planning CT, which—after applying a rotation matrix based on the gantry angle and a scaling factor based on the SID—provides an expected fiducial position on each frame. The search region centered on these expected locations is expanded by double the range of motion observed on the treatment planning 4D CT scan. For the patients in this study the range of motion was between 7 and 10 mm, so the region of interest was 14–20 mm. Figure 1 shows an example of a pair of frames using matched positions in the same arc from a patient's fraction captured using the MLI's 4-layer mode and a fraction captured using 1-layer mode. The green circles show the search area for each fiducial, the asterisks are templates generated at a fiducial's initial tracked location after a frame with unsuccessful tracking, and the blue arrows point to the corresponding templates' current tracked location.

Generating 'truth data' with which to compare the tracked fiducial locations was performed by combining external surrogate breathing data with some manually tracked images. Each treatment arc generated hundreds of image frames, so performing manual tracking on each frame was not practical. Since every patient had a breathing trace recorded during radiation delivery, we were able to use the trace as a surrogate for relative fiducial location. The correlation of surface markers with internal tumor motion has been the topic of extensive research (Gierga *et al* 2005, Ionascu *et al* 2007, Fayad *et al* 2011, Lu *et al* 2015). In our study, 14 frames near the beginning of the treatment arc and 14 frames near the end of the treatment arc were selected based on the visibility of the fiducials within the aperture. The fiducial locations in these frames were identified manually and the time points matched to the corresponding time point of the breathing trace (figure 2). In order to match the TrueBeam time stamps with the acquired images, the in-treatment triggered kV images were used to temporally match the breathing trace with the collected frames. The kV images were acquired at known recorded gantry angles, so their time stamps could be compared with the metadata time of the MV images acquired at the same gantry angle, and any discrepancy appropriately compensated for.
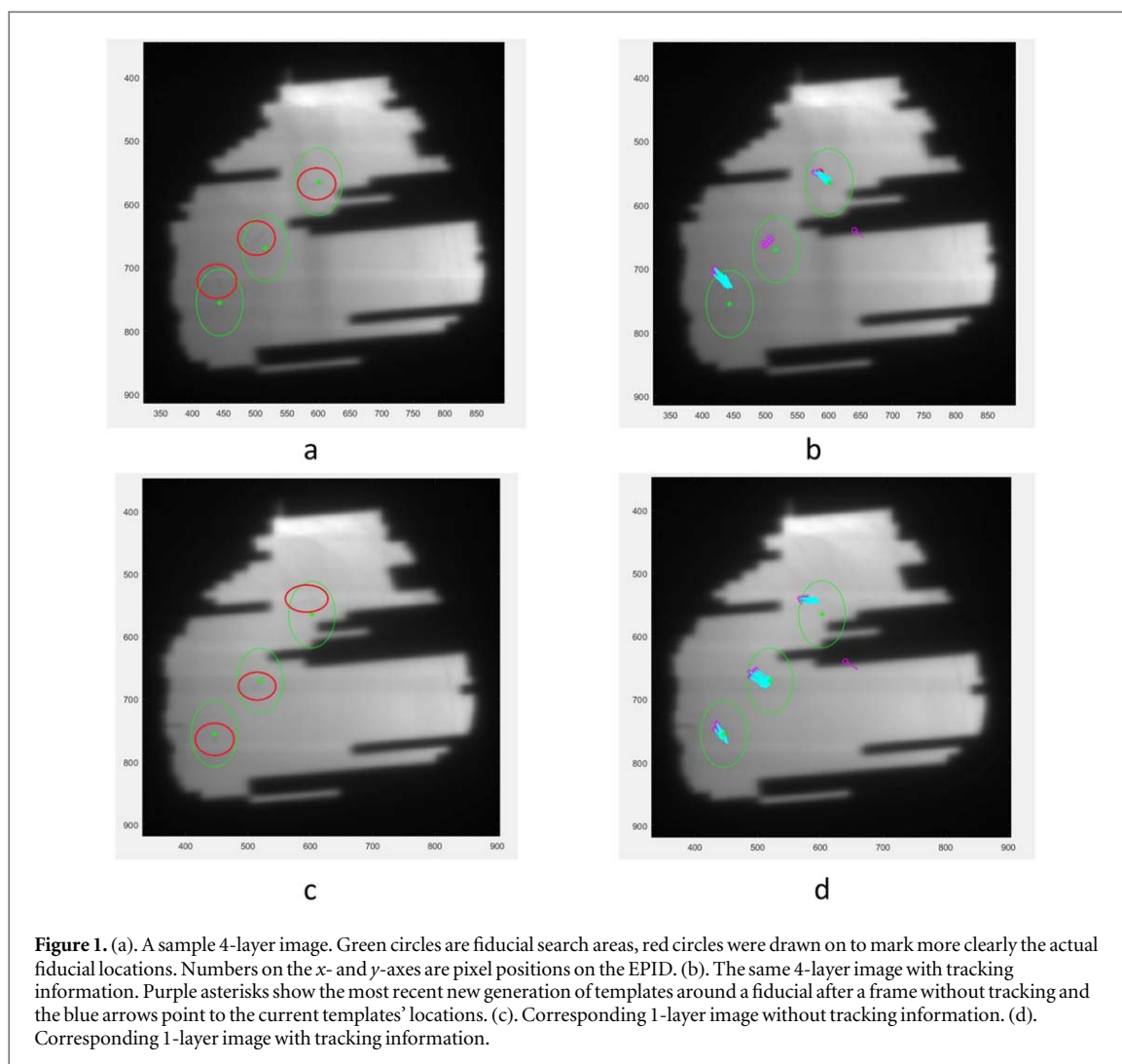
Figure 1. (a). A sample 4-layer image. Green circles are fiducial search areas, red circles were drawn on to mark more clearly the actual fiducial locations. Numbers on the *x*- and *y*-axes are pixel positions on the EPID. (b). The same 4-layer image with tracking information. Purple asterisks show the most recent new generation of templates around a fiducial after a frame without tracking and the blue arrows point to the current templates' locations. (c). Corresponding 1-layer image without tracking information. (d). Corresponding 1-layer image with tracking information.
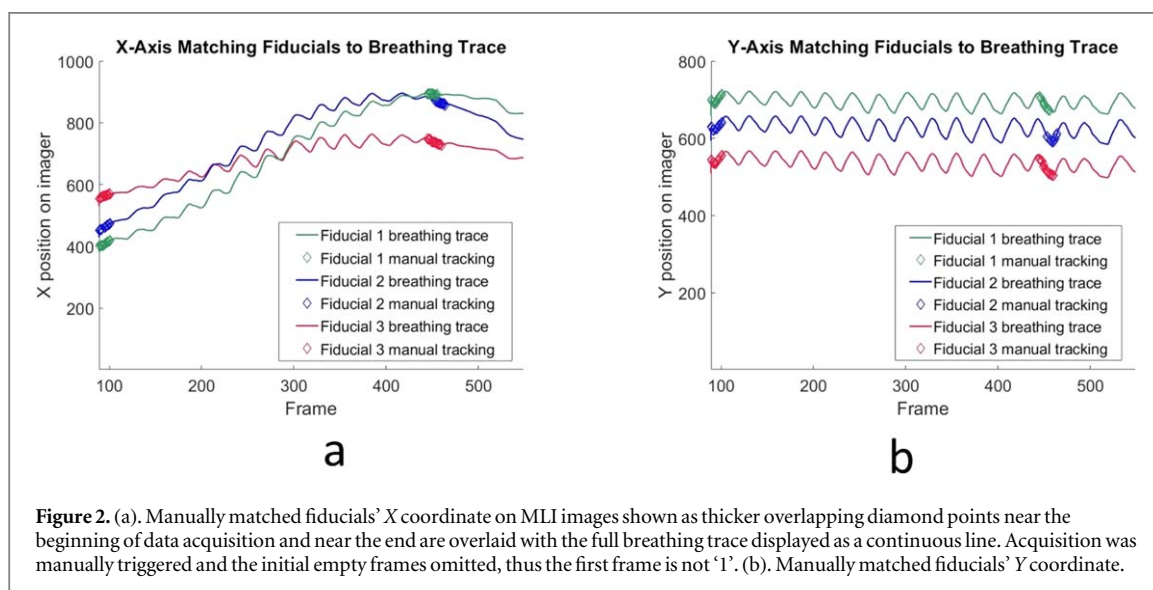

Figure 2. (a). Manually matched fiducials' *X* coordinate on MLI images shown as thicker overlapping diamond points near the beginning of data acquisition and near the end are overlaid with the full breathing trace displayed as a continuous line. Acquisition was manually triggered and the initial empty frames omitted, thus the first frame is not '1'. (b). Manually matched fiducials' *Y* coordinate.

The tracking algorithm reads in the collected images, searches for fiducials, and compares the found location to the derived truth data for error analysis. The algorithm also estimates an expected number of frames for which a fiducial might be visible by comparing the expected fiducial location at each frame with the MLC coverage for that location in that frame. The number of frames with successful tracking of a particular fiducial are compared to the theoretical maximum number of trackable frames to calculate an efficiency metric. Paired two sample for

Table 1. Tracking results for all of patients, each arc, are shown. 4-layer mode results in more accurate and more efficient tracking ($p < 0.001$).

		2D tracking error and tracking efficiency by patient arc							
		Patient 1	Patient 2	Patient 3	Patient 4	Patient 5	Patient 6	Mean	Delta
Tracking RMSE (mm)	4-layer	1.36	1.65	1.61	1.53	1.32	1.26	1.5	0.6 $p < 0.001$
	1-layer	2.11	2.28	2.52	2.03	1.80	1.76	2.1	
Tracking efficiency	4-layer	84.4%	88.7%	83.4%	79.7%	84.9%	75.2%	82.8%	41.7% $p < 0.001$
	1-layer	55.7%	64.4%	59.3%	58.3%	59.6%	55.5%	58.4%	

means T-tests were used to assess the significance of the difference in tracking error and efficiency between 1-layer acquisitions and 4-layer acquisitions.

2.4. Analysis

We studied several conditions for the differences in tracking efficiency and accuracy between the 4-layer and 1-layer modes. One hypothesis was that the tracking efficiency would be correlated with gantry angle, meaning that certain ranges of the treatment arcs were better suited for tracking, in general, and that some low efficiency angles could be improved with the 4-layer imaging. In addition, dose rate as a function of gantry angle was cataloged for all acquired frames using MU per frame as a proxy for dose rate, given that the frame grabber card acquired images at a stable 10.1 frames per second. We sought to determine if dose/frame impacted the tracking efficiency and could likewise be overcome by the 4-layer imager.

Our second main hypothesis was that image noise would be correlated to tracking efficiency such that reduction in noise would lead to better efficiency. Image noise at a particular gantry angle is a function of dose-rate of the source, radiological depth of the subject and DQE of the imaging panel. Using the same fiducial location prediction technique explained in section 2.3, the image noise in the search location of the seeds was calculated. First, a median-filtered version of each frame was subtracted from the corresponding frame to remove deterministic background non-uniformities. A 5×5 median pixel filter was used for this step, which outputs the median pixel value in a 5×5 pixel neighborhood around the input pixel. Second, the MLCs were masked on the image. Third, the image was cropped to the fiducial search area. Finally, the noise was determined from the standard deviation of the pixel values unless the MLCs obscured the data, in which case the data point was omitted. This calculation was performed for every fiducial across all of the patient image frames for both 1-layer and 4-layer cases.
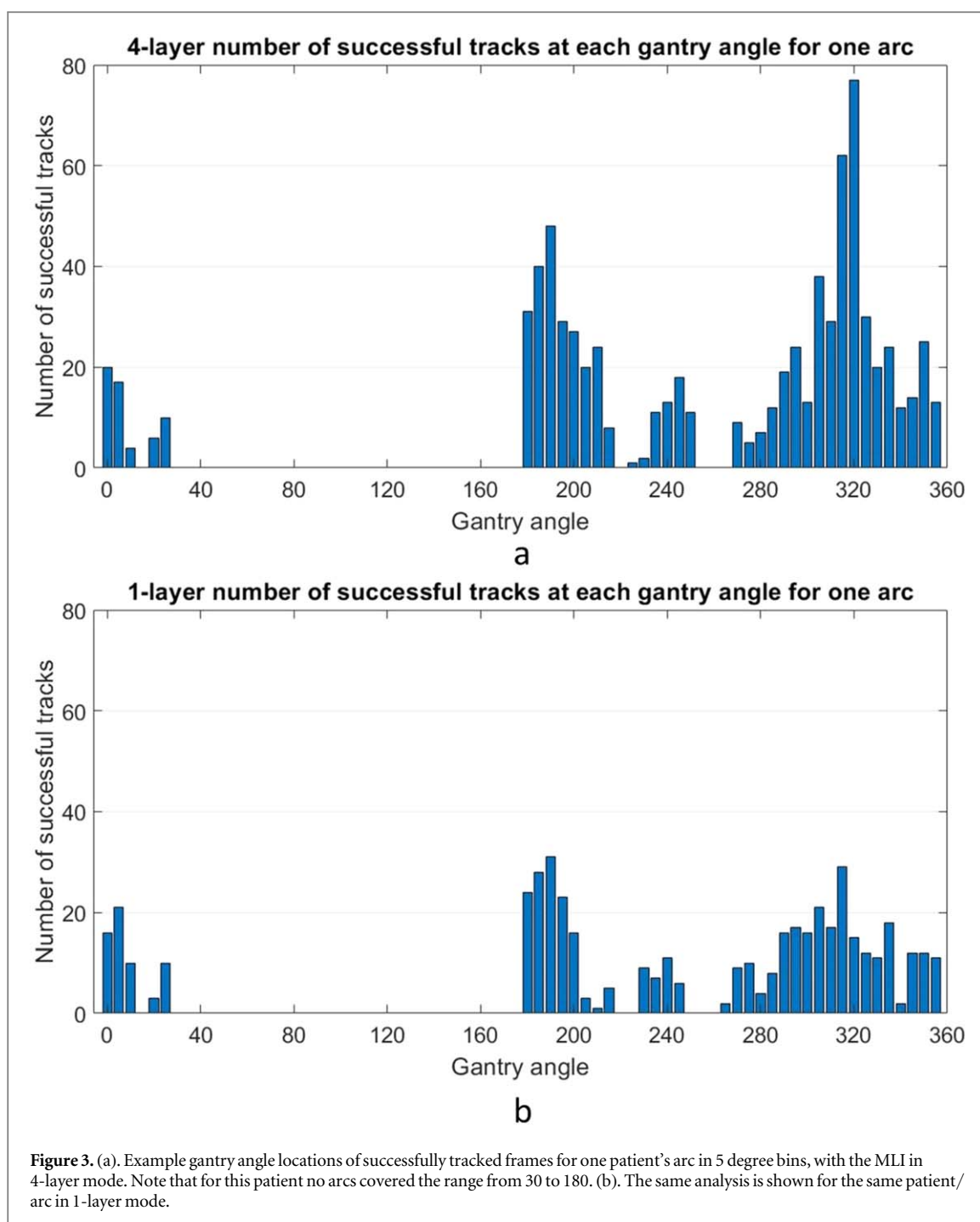
3. Results

A total of 23 242 clinical BEV MV image frames were successfully captured from the six liver SBRT patients, excluding frames that were blank due to manual triggering and gating. For each patient, data was acquired during two fractions: one fraction with the MLI in 4-layer acquisition mode and one fraction with it in 1-layer acquisition mode. Continuous saving of the image data stream was triggered manually to occur independent of the treatment status, although the tracking algorithm ignores image frames when the MV beam is not on (as defined by the BeamOn flag in each image's metadata).

The tracked position of each fiducial in each arc was compared to the truth data location and the root mean square error (RMSE) in the *X* direction, *Y* direction, and total error calculated. Including the data from all fiducials in every arc in every patient, the 1-layer RMSE was 2.1 mm and the 4-layer RMSE 1.5 mm, an improvement of 0.6 mm ($p < 0.001$). Patient by patient data is shown in table 1.
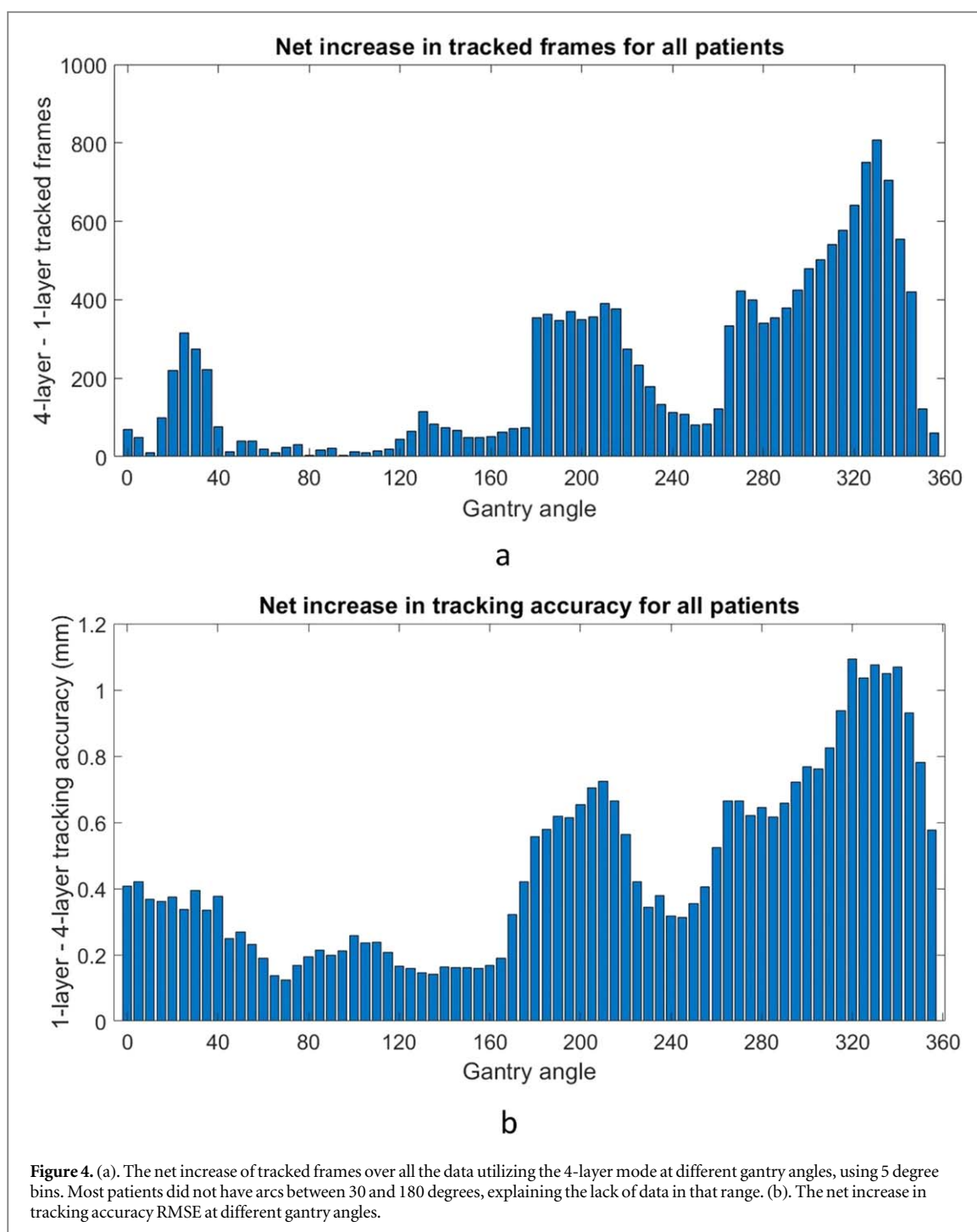
The number of successfully tracked frames of each fiducial of each arc of each patient was compared to the theoretical maximum number of frames for which tracking was possible, i.e. when at least one fiducial was not covered by the MLCs. This ratio of successful tracking frames to total frames was defined as the 'tracking efficiency'. The tracking algorithm was able to return results for 58.4% of the 1-layer data image frames and 82.8% of the 4-layer data image frames, an absolute increase of 24.4% ($p < 0.001$).

The gantry angle distribution of where successful tracking occurred was analyzed. Due to the laterality of the liver, many of the patients did not have arcs covering the range from 30 to 180 degrees. Figure 3 shows the distribution for a single arc of a patient's treatment when the MLI is in 4-layer mode and the corresponding arc in 1-layer mode. Some angles also have no tracking due to MLC interference. Of note, the increase in tracking from multi-layer acquisition does not appear homogenously distributed. The net increase of tracked frames for

Figure 3. (a). Example gantry angle locations of successfully tracked frames for one patient's arc in 5 degree bins, with the MLI in 4-layer mode. Note that for this patient no arcs covered the range from 30 to 180. (b). The same analysis is shown for the same patient/arc in 1-layer mode.

the 4-layer mode displays similar trends for all patients with a peak centered around 330 degrees gantry angle and a valley centered around 250 degrees gantry angle (figure 4).
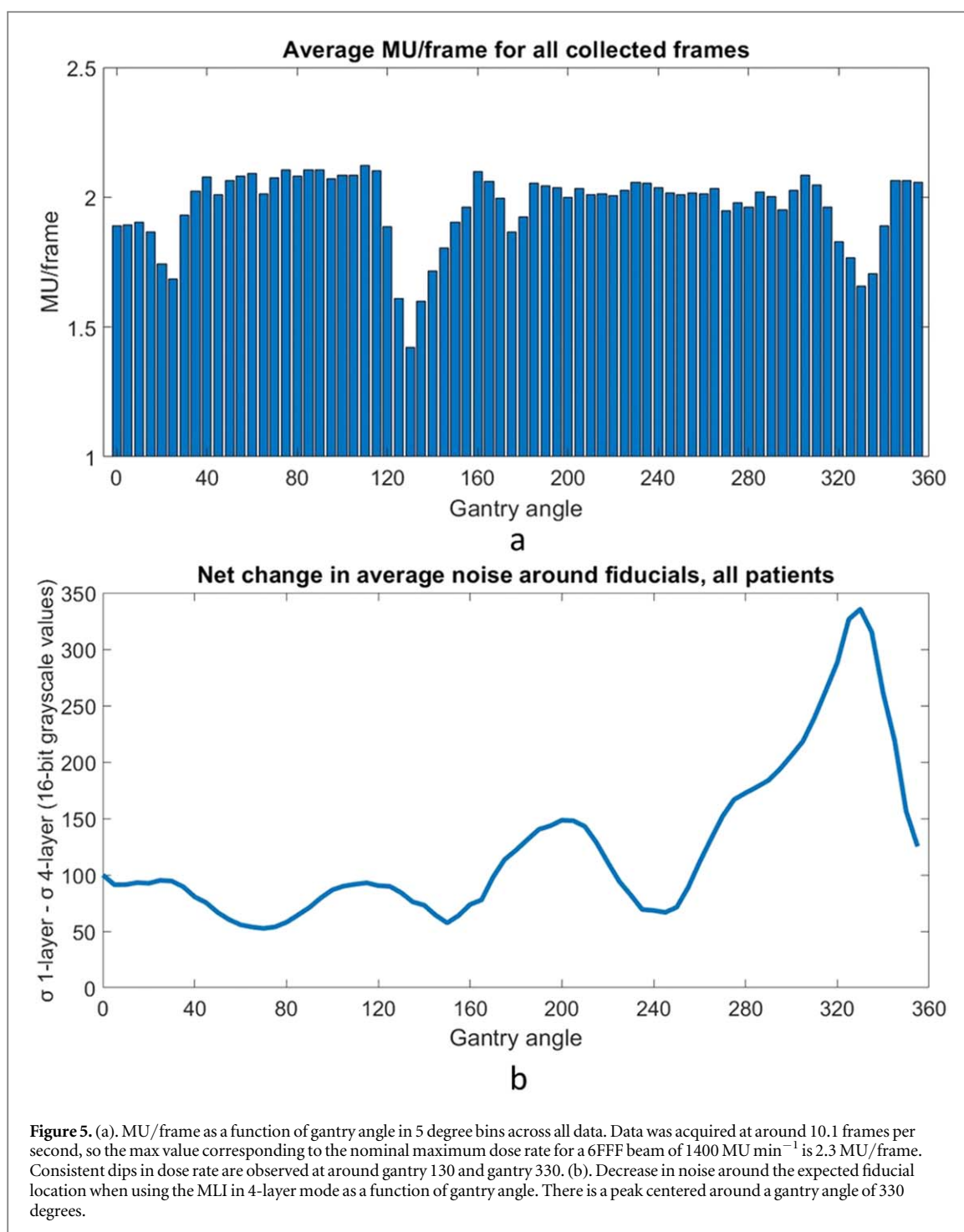
The average MU per frame as a function of gantry angle was evaluated for all collected frames in the cohort of patients (figure 5(a)). The frame grabber acquired images at a stable rate of 10.1 frames per second, meaning the maximum MU per frame is roughly 2.3, given the nominal 6FFF dose rate of 1400 MU min^{-1}. The delivered dose rate was stable except for noticeable dips near gantry 30, 130, and 330. The image noise in the search region around each fiducial across all data was determined as described in section 2.4. Data from fiducials obscured by MLCs were omitted and defined as 'untrackable'. The average decrease noise as a function of gantry angle is shown in figure 5(b). There is a peak centered around the gantry angle of 330 degrees. Figure 6 combines the plots of the net tracking increase by gantry angle and the noise per gantry angle. There is a strong correlation between image noise and improved tracking with the 4-layer mode of MLI ($r = 0.913$). The correlation is also strong ($r = 0.927$) when considering the relationship between image noise and tracking accuracy improvement. Figure 7 replots figures 6(a) and (b) as a function of noise decrease instead of gantry angle.

Figure 4. (a). The net increase of tracked frames over all the data utilizing the 4-layer mode at different gantry angles, using 5 degree bins. Most patients did not have arcs between 30 and 180 degrees, explaining the lack of data in that range. (b). The net increase in tracking accuracy RMSE at different gantry angles.

4. Discussion

The 4-layer MLI provides statistically significant improvement in tracking accuracy and efficiency versus 1-layer acquisition. Previous work has shown that tracking performance is generally limited by quantum noise, which is dominated by DQE (Hu *et al* 2017). This is demonstrated in the superior tracking performance of the higher DQE imaging mode, i.e. 4-layer acquisition. The more than five-fold increase in DQE, utilizing four layers, led to a 41.7% relative increase in tracking efficiency and statistically significant increase in tracking accuracy, as well. Future studies could investigate fiducials of different diameters and lengths, as well as other marker types such as gold anchors.

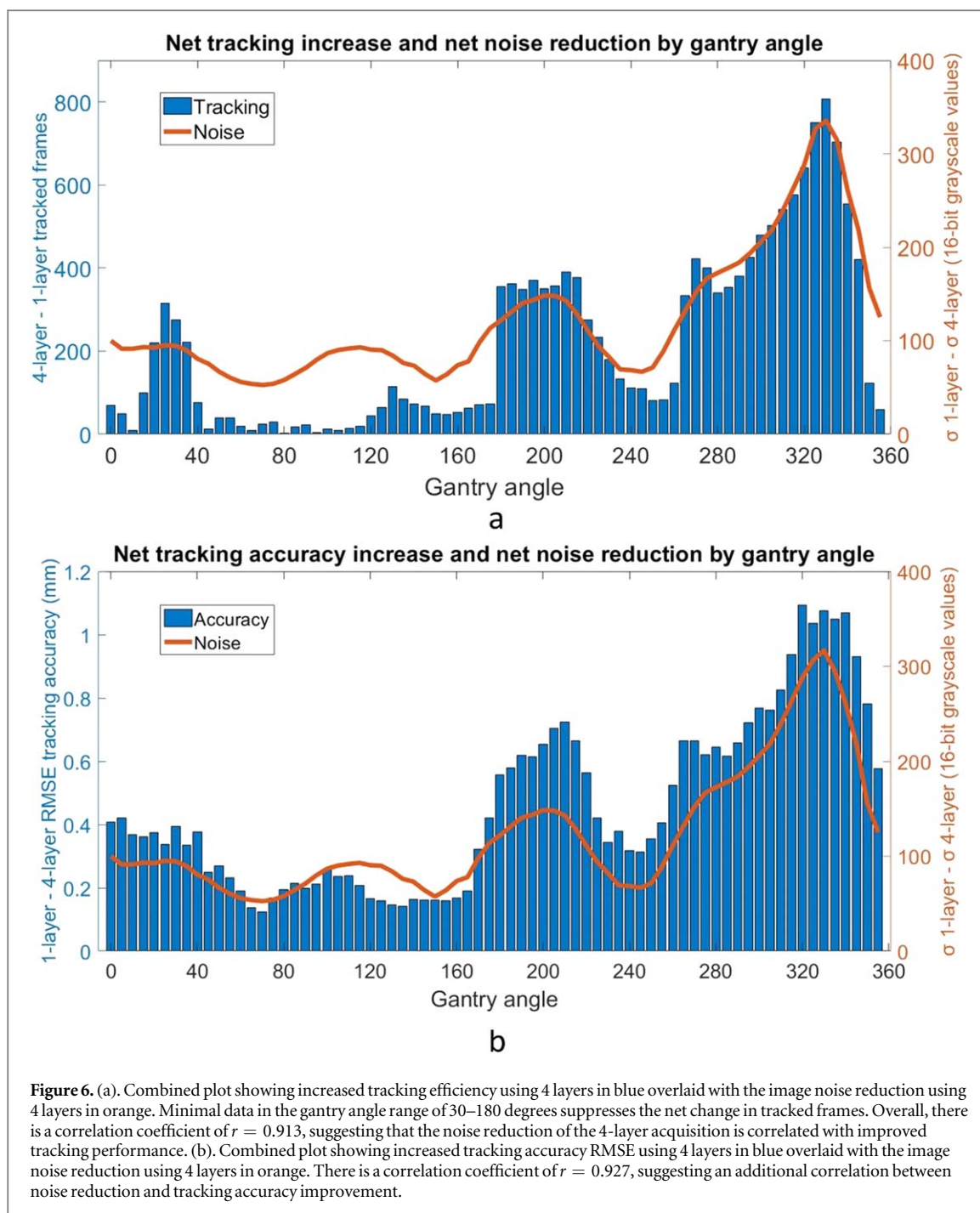As discussed in prior work by our group (Harris *et al* 2020), improved tracking performance is primarily driven by improved noise power spectrum, with the minor decrease in modulation transfer function having negligible impact on the ability to track fiducials. However, creating a single layer EPID with a GOS layer four times thicker likely would not yield similar results. A prior study demonstrated decreasing returns for GOS

Figure 5. (a). MU/frame as a function of gantry angle in 5 degree bins across all data. Data was acquired at around 10.1 frames per second, so the max value corresponding to the nominal maximum dose rate for a 6FFF beam of 1400 MU min^{-1} is 2.3 MU/frame. Consistent dips in dose rate are observed at around gantry 130 and gantry 330. (b). Decrease in noise around the expected fiducial location when using the MLI in 4-layer mode as a function of gantry angle. There is a peak centered around a gantry angle of 330 degrees.

layers thicker than 0.500 mm, due to signal power degradation offsetting the decrease in noise power (Hu *et al* 2017). Furthermore, a thicker scintillator layer creates additional optical photon spread, leading to optical Swank noise (Swank 1973). The MLI architecture used in this study allows an effectively thicker scintillator without increased optical Swank noise.

MLI may offer the additional advantage of detecting errors in patient positioning. For example, during patient treatment for this study, there was one fraction during 4-layer acquisition when an unacceptable change in position was detected on the treatment console using the triggered-kV images, so the MV frame grabber was halted during the repeat CBCT and then re-started for the acquisition of the remainder of that arc. The two parts of the arc were later stitched together. The MV data for this particular arc was later reviewed, and one of the three fiducials was visible in frame when the kV images detected a misalignment. The fiducial position was being tracked with an accuracy or 1.1 mm or less, suggesting that the MLI may have detected the setup issue as well.
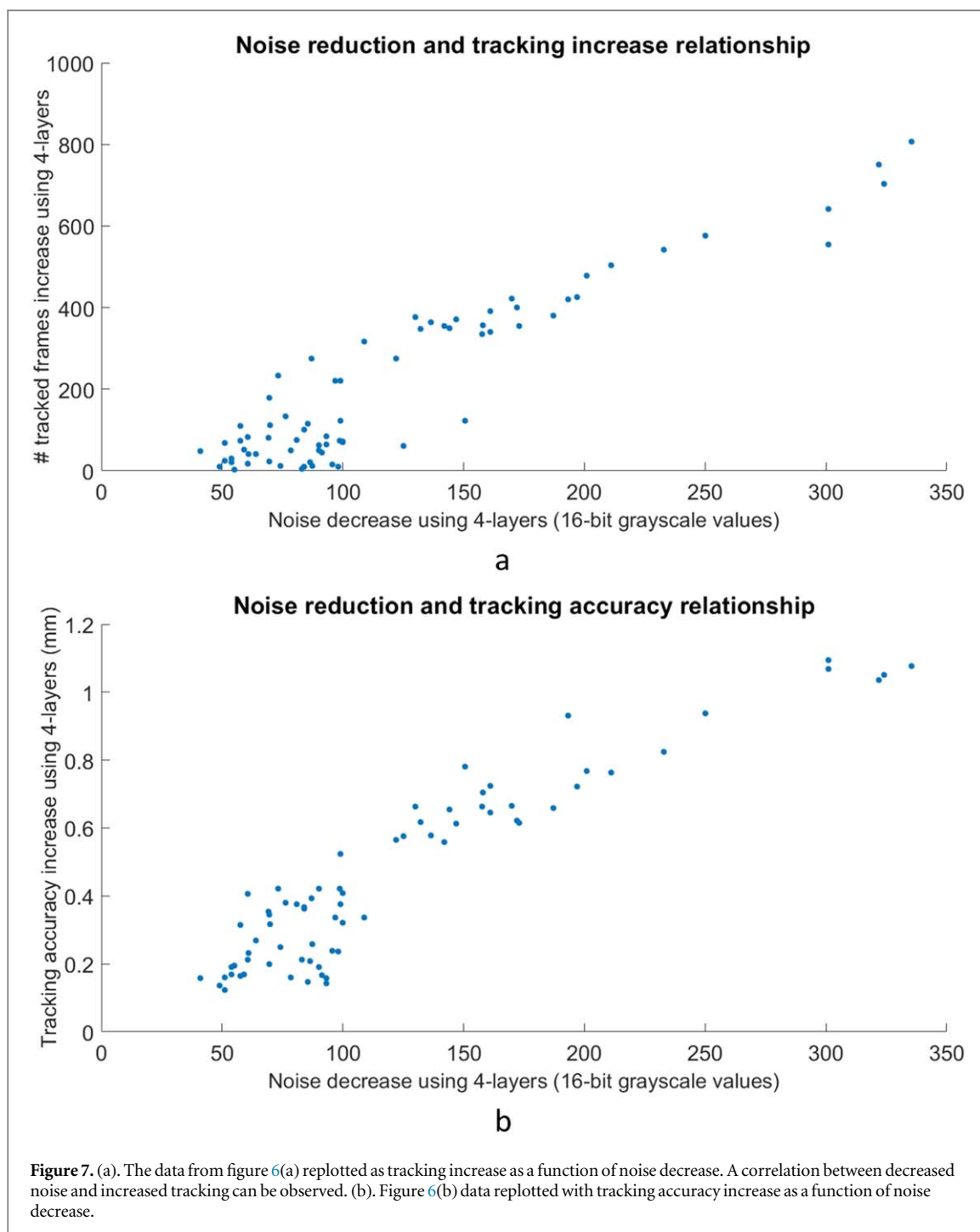
A pattern of greatly improved tracking with the 4-layer mode around a gantry angle of 330 degrees emerged during the analysis (figure 6). Investigating this further, it was noted that the treatment beams often pass through

Figure 6. (a). Combined plot showing increased tracking efficiency using 4 layers in blue overlaid with the image noise reduction using 4 layers in orange. Minimal data in the gantry angle range of 30–180 degrees suppresses the net change in tracked frames. Overall, there is a correlation coefficient of $r = 0.913$, suggesting that the noise reduction of the 4-layer acquisition is correlated with improved tracking performance. (b). Combined plot showing increased tracking accuracy RMSE using 4 layers in blue overlaid with the image noise reduction using 4 layers in orange. There is a correlation coefficient of $r = 0.927$, suggesting an additional correlation between noise reduction and tracking accuracy improvement.

both the fiducials and the spine from this direction. The MLCs tend to be close to the fiducials, blocking the spine when possible. This condition likely results in relatively higher image noise, which would limit tracking with the 1-layer mode more than with the 4-layer mode.

Across all of the gantry angles, in regions where there is more noise around the fiducials, the 4-layer panel is able to track more frames than the 1-layer mode. In angular regions where there is less noise in the images and tracking is relatively easier, the advantage of higher detector efficiency is less prominent. Figure 7 suggests that for the tracking system analyzed in this study, there may be a threshold in noise improvement needed before performance increases. Performance improvements appear to taper off as noise decreases, likely reflecting that accuracy and efficiency can only be improved so much. More data is needed for further quantification, and more tracking systems would need to be studied before generalizing this observation.

Monitoring of intrafraction target motion can improve treatment delivery accuracy for radiation therapy (Bertholet *et al* 2019), particularly in anatomical regions sensitive to respiratory motion (Keall *et al* 2006). Without active monitoring, there are other strategies to address target motion. For example, a 4D CT can help quantify the typical range of intrafraction motion (Mageras *et al* 2004) but does not provide information at the

Figure 7. (a). The data from figure 6(a) replotted as tracking increase as a function of noise decrease. A correlation between decreased noise and increased tracking can be observed. (b). Figure 6(b) data replotted with tracking accuracy increase as a function of noise decrease.

time of treatment. Methods for minimizing motion include active breathing control (Wong *et al* 1999), various breath hold methods (Boda-Heggemann *et al* 2016), and abdominal compression (Heinzerling *et al* 2008). However, these tools do not provide feedback on the actual target position and motion during treatment.

BEV imaging with the MV beam during treatment delivery can be used to verify the above methods of motion mitigation without contributing additional imaging dose to the patient. In-treatment patient imaging with current conventional MV imagers has drawbacks, however, such as poor contrast and DQE, making clinical adoption challenging. Additionally, MLC modulation and gantry rotation during beam delivery further complicate fiducial identification. In this study, we have sought to demonstrate that increased photon detection efficiency through detector modifications reduces image noise and thereby improves both tracking efficiency and tracking accuracy. While the 4-layer MLI used in the study has achieved those goals, other innovations will be necessary in order to overcome remaining challenges, such as MLC obstructions.

5. Conclusion

BEV imaging with a novel MLI demonstrated increased tracking efficiency and tracking accuracy compared to a reference single layer imager for clinical liver SBRT treatments. The improved performance is highly correlated with the reduction in image noise associated with the photon detection efficiency of each imaging panel. For future innovations, including MV imaging to monitor radiotherapy treatments, incorporating high efficiency detectors, like the MLI used in this study, is recommended.

Acknowledgments

ORCID iDs

T C Harris ⓘ https://orcid.org/0000-0002-5594-5728
I Valencia Lozano ⓘ https://orcid.org/0000-0002-9130-8590

References

Antonuk L E 2002 Electronic portal imaging devices: a review and historical perspective of contemporary technologies and research *Phys. Med. Biol.* **47** R31–65

Azcona J D, Li R, Mok E, Hancock S and Xing L 2013 Development and clinical evaluation of automatic fiducial detection for tumor tracking in cine megavoltage images during volumetric modulated arc therapy *Med. Phys.* **40** 031708

Bertholet J *et al* 2019 Real-time intrafraction motion monitoring in external beam radiotherapy *Phys. Med. Biol.* **64** 15TR01

Boda-Heggemann J *et al* 2016 Deep inspiration breath hold-based radiation therapy: a clinical review *Int. J. Radiat. Oncol. Biol. Phys.* **94** 478–92

Cho B, Poulsen P R, Sawant A, Ruan D and Keall J 2011 Real-time target position estimation using stereoscopic kilovoltage/megavoltage imaging and external respiratory monitoring for dynamic multileaf collimator tracking *Int. J. Radiat. Oncol. Biol. Phys.* **79** 269–78

Fayad H, Pan T, Clement J F and Visvikis D 2011 Technical note: correlation of respiratory motion between external patient surface and internal anatomical landmarks *Med. Phys.* **38** 3157–64

Ferguson D *et al* 2020 Markerless tumor tracking for VMAT *Phys. Med. Biol.* **65** 125011

Gierga D P, Brewer J, Sharp G C, Betke M, Willett C G and Chen G T Y 2005 The correlation between internal and external markers for abdominal tumors: implications for respiratory gating *Int. J. Radiat. Oncol. Biol. Phys.* **61** 1551–8

Happersett L, Wang P, Zhang P, Mechalakos J, Li G, Eley E, Zelefsky M, Mageras G, Damato A L and Hunt M 2019 Developing a MLC modifier program to improve fiducial detection for MV/kV imaging during hypofractionated prostate volumetric modulated arc therapy *J. Appl. Clin. Med. Phys.* **20** 120–4

Harris T C *et al* 2020 Clinical translation of a new flat-panel detector for beam's-eye-view imaging *Phys. Med. Biol.* **65** 225004

Heinzerling J H, Anderson J F, Papiez L, Boike T, Chien S, Geoffrey Z, Abdulrahman R and Timmerman R 2008 Four-dimensional computed tomography scan analysis of tumor and organ motion at varying levels of abdominal compression during stereotactic treatment of lung and liver *Int. J. Radiat. Oncol. Biol. Phys.* **70** 1571–8

Herman M G, Balter J M, Jaffray D A, McGee K P, Munro P, Shalev S, Van Herk M and Wong J W 2001 Clinical use of electronic portal imaging: report of AAPM radiation therapy committee task group 58 *Med. Phys.* **28** 712–37

Hu Y H *et al* 2018 Feasibility of closed-MLC tracking using high sensitivity and multi-layer electronic portal imagers *Phys. Med. Biol.* **63** 235030

Hu Y H, Myronakis M, Rottmann J, Wang A, Morf D, Shedlock D, Baturin P, Star-Lack J and Berbeco R 2017 A novel method for quantification of beam's-eye-view tumor tracking performance *Med. Phys.* **44** 5650–9

Hu Y H *et al* 2019 Characterizing a novel scintillating glass for application to megavoltage cone-beam computed tomography *Med. Phys.* **46** 1323–30

Ionascu D, Jiang S B, Nishioka S, Shirato H and Berbeco R I 2007 Internal-external correlation investigations of respiratory induced motion of lung tumors *Med. Phys.* **34** 3893–903

Keall P, Todor A D, Vedam S S, Bartee C L, Siebers J V, Kini V R and Mohan R 2004 On the use of EPID-based implanted marker tracking for 4D radiotherapy *Med. Phys.* **31** 3492–9

Keall P J *et al* 2006 The management of respiratory motion in radiation oncology report of AAPM task group 76 *Med. Phys.* **33** 3874–900

Lu B, Chen Y, Park J C, Fan Q, Kahler D and Liu C 2015 A method of surface marker location optimization for tumor motion estimation in lung stereotactic body radiation therapy *Med. Phys.* **42** 244–53

Ma T, Kilian-Meneghin J and Kumaraswamy L 2018 Recommendation of fiducial marker implantation for better target tracking using MV imager in prostate radiotherapy *J. Appl. Clin. Med. Phys.* **19** 389–97

Mageras G S *et al* 2004 Measurement of lung tumor motion using respiration-correlated CT *Int. J. Radiat. Oncol. Biol. Phys.* **60** 933–41

Murphy M J *et al* 2007 The management of imaging dose during image-guided radiotherapy: report of the AAPM Task Group 75 *Med. Phys.* **34** 4041–63

Park S-J, Ionascu D, Hacker F, Mamon H and Berbeco R 2009 Automatic marker detection and 3D position reconstruction using cine EPID images for SBRT verification *Med. Phys.* **36** 4536–46

Star-Lack J *et al* 2015 A piecewise-focused high DQE detector for MV imaging *Med. Phys.* **42** 5084–99

Swank R K 1973 Absorption and noise in x-ray phosphors *J. Appl. Phys.* **44** 4199–203

Wiersma R D, Mao W and Xing L 2008 Combined kV and MV imaging for real-time tracking of implanted fiducial markers *Med. Phys.* **35** 1191–8

Wong J W, Sharpe M B, Jaffray D A, Kini V R, Robertson J M, Stromberg J S and Martinez A A 1999 The use of active breathing control (ABC) to reduce margin for breathing motion *Int. J. Radiat. Oncol. Biol. Phys.* **44** 911–9

Yue Y, Aristophanous M, Rottmann J and Berbeco R I 2011 3-D fiducial motion tracking using limited MV projections in arc therapy *Med. Phys.* **38** 3222–31

Zhao W, Ristic G and Rowlands J A 2004 X-ray imaging performance of structured cesium iodide scintillators *Med. Phys.* **31** 2594–605

Chapter 3

Discussion

3.1 Tumor tracking advances

The algorithm described in chapter 2.1 tracks tumor motion without implanted markers using only MV EPID images.   Our development is novel in that it tracks the tumor during volumetric modulated arc therapy (VMAT) by using the MV treatment beam. VMAT is a relatively new method of delivering radiation therapy; previously, radiation treatments were delivered using fixed gantry positions with static fluences.   Tumor tracking during these treatments was relatively easy, as the only motion would come from the patient and the field aperture generally encompassed the whole target.   Now, however, treatments can be delivered while the gantry is rotating around the patient with the radiation fluence constantly changing, a technique called VMAT (Otto 2008).   While VMAT can beneficially avoid irradiating healthy organs, the fluence at a particular point in time may also obscure a considerable amount of the target.

One strategy for verifying tumor location is the use of fiducial markers – small, radio-opaque, high-Z materials (typically gold) surgically implanted into the tumor (Shirato *et al.* 2003).   However, while smaller than the tumor, these markers may still become obscured from the EPID during VMAT delivery.   The created tracking algorithm addresses this challenge by, instead of tracking an implanted fiducial marker, tracking on areas of high variance in the pixel values, which indicate presence of some sort of feature such as a boundary (like the interface between a lung tumor and the surrounding lung tissue) or a high-density nodule.   The algorithm is able to incorporate such features as they come into the BEV and discard them when they exit.

A review of available literature suggests that, to our knowledge, this algorithm is the first of its kind to demonstrate markerless tumor tracking using MV images collected during VMAT treatments.   In addition, this algorithm provides a test

application for a later portion of the thesis when evaluating the performance of a multilayer EPID versus a single layer imager.

3.2   EPID architecture advances

A prototype megavoltage multilayer imager was tested and clinically deployed. This is the first time an EPID utilizing such architecture has been shown to be not only functional in a clinical setting, but an improvement over a standard imager.

Briefly, an EPID is typically comprised of three layers.   A sheet of copper converts incoming photons into secondary electrons; a scintillator (often gadolinium oxysulfide) converts the electrons to optical photons; and an array of photodiode thin film transistors (TFT) detects the optical photons.   As described in chapter 1.1, the motive for designing improved EPIDs is to overcome their poor performance, in particular with regards to contrast and detection efficiency.   Considerable research has been directed to this aim, often focusing on the scintillator layer.   Different materials such as a novel glass (Hu *et al.* 2019) and different construction of the layer (Star-Lack *et al.* 2015) have shown promise.   However, these approaches are costly and difficult to manufacture, making widespread adoption challenging.
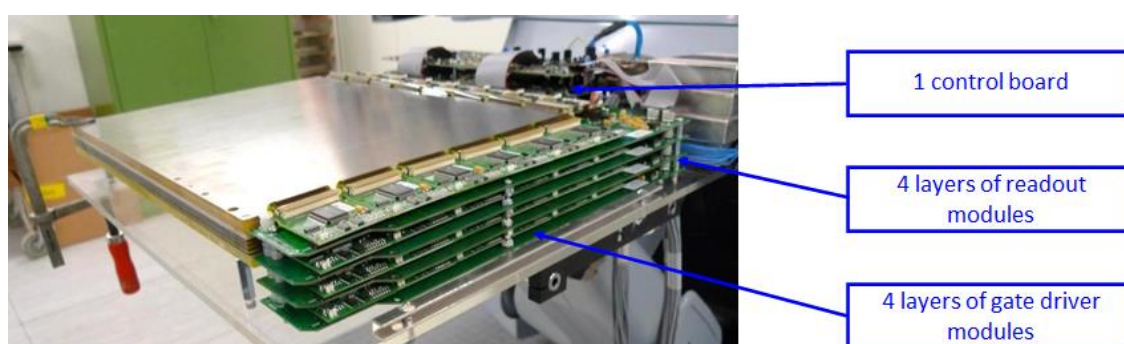

Figure 3: the MLI with its cover removed, showing the four layers of electronics.

Simply increasing the scintillator thickness to increase detection efficiency is not a viable option.   As thickness increases, so does the optical photon path length to the TFT, magnifying any optical spread, increasing optical Swank noise, and

reducing signal power, which particularly becomes an issue when thickness exceeds 0.500 mm (Hu *et al.* 2017).   The approach taken in our work aimed to effectively increase the scintillator thickness without increased optical spread by vertically stacking four layers of a standard EPID (Figure 3).   This approach allowed more photons from the beam to be sampled while preserving spatial resolution.   Each scintillator layer thickness was also increased from the standard 0.290 mm to 0.436 mm, attempting to increase photon detection while keeping the thickness below the point of diminishing returns.

Image noise is related to the number of detected photons N by $1/\sqrt{N}$, so if the number of detected photons is quadrupled one would expect noise to be halved.   Figure 4 shows the results of irradiating a standard imaging phantom and calculating the CNR and SNR.   The four layer MLI is observed to have nearly double the CNR and SNR of the single layer MLI, and an even greater increase over a standard reference EPID.   Qualitatively, one can also observe that the four layer image is less noisy.
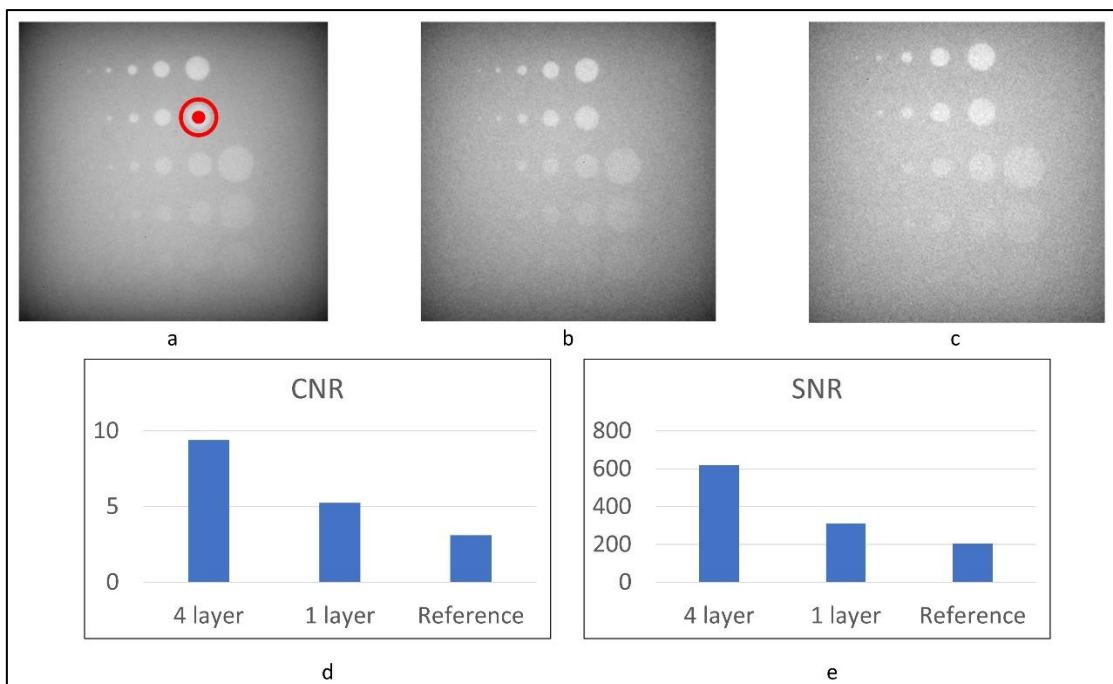

Figure 4. a. Las Vegas imaging phantom imaged using 4 layer MLI.   Signal is the red circle and background calculations use the red annulus.   b. Using 1 layer MLI.   c. Using a standard reference EPID.   d. CNR comparison of the three images.   e. SNR comparison of the three images.

Utilizing standard imaging layers is an important way of reducing the complexity and cost of widespread adoption. The panel's electronics were redesigned in order to ensure that the MLI would fit in the same housing as a standard EPID as well as to address increased heat generation from the four layers. We inserted boards with aluminum cooling elements, which transferred heat using thermal pads. These cooling elements were then air-cooled using fans. The extra layers and electronics increased the mass of the EPID to 24.7 kg, compared to a standard EPID's 18.0 kg. Prior to its use, the panel was tested on a non-clinical linear accelerator to ensure that the additional weight would not damage the gantry's mounting arm. The prototype panel proved robust for the duration of the experiment and had been continuously installed on a clinical linear accelerator for six months without any technical issues.

Multilayer architecture for EPIDs exhibits better performance, is durable for day-to-day clinic use, and is relatively simple to construct as it uses existing or slightly modified imaging components and electronics. Furthermore, the core concept readily facilitates investigation into variations. For example, fellow researchers are already studying whether further improvements are attainable by mixing different materials amongst the four layers such as the novel glass scintillator described by Hu (2019), or by weighting the contributions from each layer non-uniformly (Valencia Lozano *et al.* 2021).

3.3 Clinical application performance advances

Having demonstrated that the prototype four layer imager performs better on standard imaging tests, our next goal was to determine if these improvements would translate to clinical care. A review of the literature suggests that even when new EPID designs are constructed, the working prototypes are very rarely actually tested by running performance tests on actual human cancer patients. The clinical trial detailed in the published manuscript reprinted in chapter 2.3 revealed that the MLI's increased performance was also observable in real-life clinical situations. Imaging performance tests use standard phantoms in controlled situations, whereas individual human anatomy can vary significantly, both between different patients and in the same patient on different days. (For

example, a prostate patient's bladder and rectum might be full one day and empty the next at treatment time, creating a different internal arrangement of the tumor and nearby organs at risk.)   It is not self-evident that increased performance on image testing metrics translate identically to clinical imaging applications on patients.

The tumor tracking algorithm designed in chapter 2.1 is ideally suited to test the clinical performance of the prototype MLI.   Tumor motion during therapy, most often caused by respiration, is important to characterize and take into account, given the small margins and steep dose gradients from tumor to healthy tissue found in VMAT-delivered stereotactic body radiation therapy (SBRT) (Atkins *et al.* 2015).   However, the changing nature of patients' bodies means that the ground truth of tumor position is impossible to know, necessitating a modification of the code.   Instead of performing markerless tumor tracking, the algorithm was redesigned to detect the distinct shape and signal of gold fiducials – and only fiducials, no other anatomic features – for tracking.   The redesign was fairly straight forward, as gold fiducials already create areas of high variance on images.   The reason for this change is that a person can manually review data and mark fiducial location, creating a ground truth for use in assessing the tracking algorithm's accuracy.   Patients receiving SBRT as treatment for liver metastases routinely have gold fiducials placed in or near their tumors, which can aid in both initial patient setup (Murphy 2002) as well as observing intrafraction motion (Xu *et al.* 2014), so standard clinical care did not have to be altered to accommodate the clinical trial.

Patient data was acquired using the four layer MLI as well as a single layer EPID for comparison.   Patients all received VMAT radiation with the EPID extended into position, acquiring data for later analysis by the modified tracking algorithm.   The first metric used for comparison was tracking accuracy, as defined as the root mean square error (RMSE) of the tracked fiducial location compared to the ground truth data.   The second metric was the tracking efficiency, defined as the acquired frames where tracking was successful as a percentage of the frames where tracking might have been possible.   Not every acquired frame can have a possible successful tracking event, as any fiducial outside of the beam's aperture is obscured.

Multilayer EPID architecture demonstrated statistically significant and clinically relevant improvement over a standard single layer imager. The MLI tracking RMSE was 1.5 mm compared to 2.1 mm for single layer (p < 0.001). Increased accuracy coupled with real-time treatment monitoring allows the treatment margin added around the tumor for uncertainty to be reduced, leading to decreased irradiated healthy tissue and fewer complications for patients undergoing radiotherapy.

The second metric, tracking efficiency, was also found to be substantially improved with a relative increase of 42% (p < 0.001) in frames successfully tracked by the MLI. Whenever there is no data about the current location of the fiducials, the uncertainty has to be ameliorated by increasing the margin added to the gross tumor, leading to increased radiation dose to healthy tissue. The MLI provides increased certainty and accuracy for tumor tracking.

3.4 Further investigation into source of improvement

In addition to testing the prototype imager on the tumor tracking clinical application, the acquired data were analyzed to see if there were any possible explanations for the improved performance, which may suggest that other tasks in addition to tracking may benefit. Given the dramatic increase in CNR noted in the initial testing of the EPID (Figure 4), it was hypothesized that noise reduction may be related to increased performance. Figure 5 shows a plot relating the average increase in tracking accuracy and average decrease in noise as a function of gantry angle.
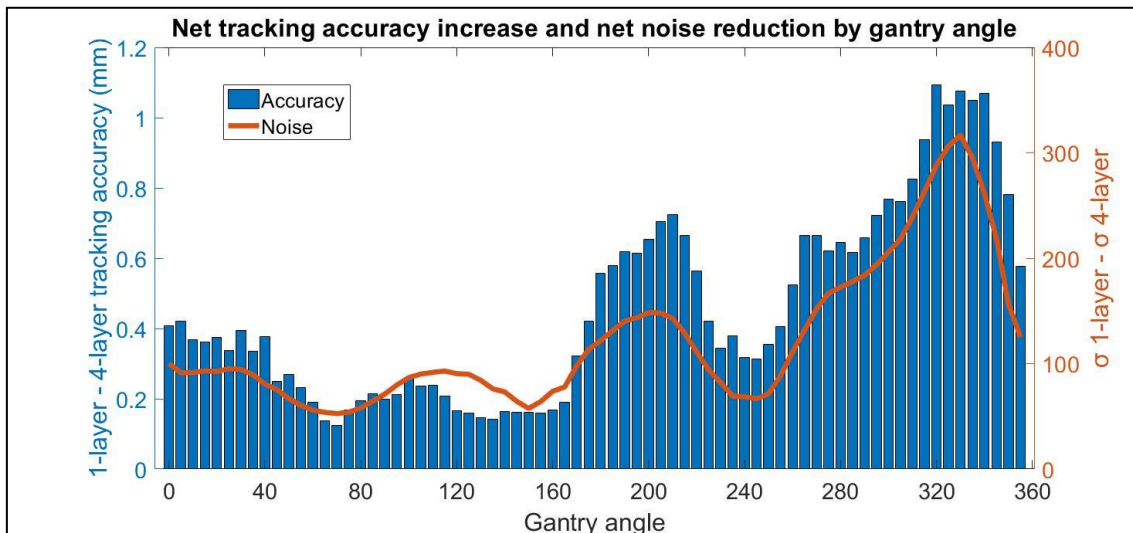
Figure 5: A plot averaged across all patients of the increase in tracking accuracy (in blue) and the decrease in noise (in orange) as a function of gantry angle. There is a correlation coefficient of r = 0.927.

Qualitatively the two plots look fairly similar, and the calculated correlation coefficient r is 0.927, suggesting that there is a relationship between noise reduction and better tracking.   Notably, there is not a uniform improvement at all angles but there are several peaks, with a particularly large one centered around a gantry angle of 320 degrees.   As the liver is a right-sided organ, radiation beams aimed at it with a setting of around 320 degrees will typically exit through the patient's spinal cord.   Due to a need to protect this critical organ from excess dose (which can lead to paralysis) (Kirkpatrick *et al.* 2010), beams at this gantry angle: 1. may be highly modulated to protect the spinal cord and 2. will traverse thicker, higher density materials (e.g., bone), both of which will increase the noise of any resultant image.   What may explain the structure of the plots in Figure 5 is that, due to patient anatomy and treatment planning concerns, certain angles are prone to be noisier at baseline, and thus see a greater absolute reduction in noise when using the MLI.   Fiducials in those noisy regions may have been more difficult for the algorithm to track with one layer images, but can be more accurately tracked once provided four layer image data.
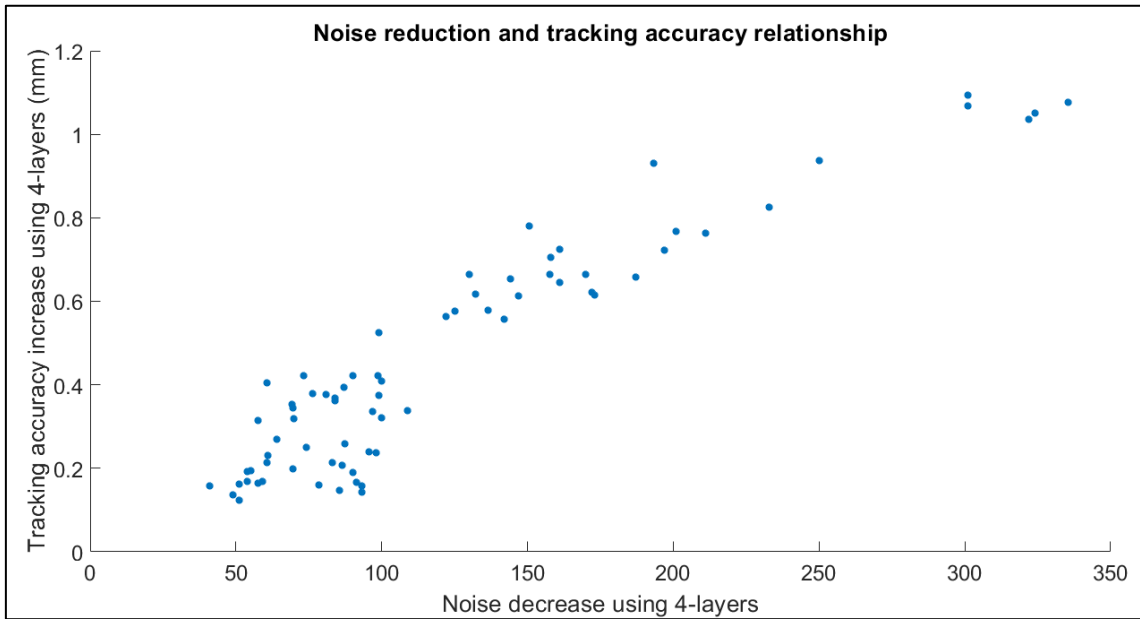
Figure 6: Tracking and noise data related but with the gantry angle axis removed.

Figure 6 shows the same data in a different way, plotting the noise and tracking data in for each 5 degree gantry angle bin, without the gantry angle as an axis. The tracking data analysis shows a clear correlation between noise reduction and improved tracking.   The initial analysis appears to show that the relationship may not be strictly linear, but rather that the effect of greater noise reduction may see some diminishing returns in extra tracking accuracy. However, more experiments are needed before reaching such a conclusion.

Chapter 4

Summary

This thesis presented a series of studies developing, testing, and clinically deploying a novel EPID architecture prototype. In the process, we were able to demonstrate its superior parameters in comparison with current EPID architecture.

The work can be broken down into three separate categories each building up to the final result.   First, a beam's-eye-view tumor tracking algorithm was developed so that the EPID would have a modern and clinically relevant application available for testing.   Second, the prototype imager was characterized using standard imaging metrics and tested on an anthropomorphic phantom.   Finally, the panel was used clinically to acquire and analyze actual patient data.

The publication in chapter 2.1 detailed the development of the tumor tracking code using MV EPID images.   The algorithm was specifically designed to accommodate contemporary complex VMAT treatments -- the first of its kind to do so.   The tracking accuracy was found to be comparable to established values previously determined for the simpler 3D conformal treatments.   The novel algorithm would later be used as a basis of comparison for the novel MLI and a single layer imager.

The MLI itself is introduced in chapter 2.2's manuscript.   The characterization tests confirmed that the MLI outperforms a standard EPID, in that a slight decrease in MTF is offset by a 5.7x increase in DQE(0) and a doubling of the CNR and SNR.   The improved performance was also observed when testing the imager on mimicked human anatomy in an anthropomorphic phantom.   For example, the CNR and SNR calculated in these images was also nearly double when using the four layer imager.

Having confirmed the MLI's improved performance, the final step was to assess

the extent to which these superior imaging parameters affected a clinical application employed on actual patients.   To that end a clinical trial – detailed in chapter 2.3 – was conducted on patients with liver metastases.   Data were acquired during their VMAT therapy delivery across two separate treatments: one using the four layer MLI and one using a single layer imager.   The acquired frames were analyzed by a modified version of the algorithm presented in chapter 2.1, and the difference between the 4 layer and single layer results were evaluated.   The four layer results showed a relative tracking efficiency improvement of 42% and a decrease in the tracking accuracy RMSE from 2.1 mm to 1.5 mm as compared to the single layer results.   These results confirm that the MLI's enhanced imaging materially improves systems used to monitor radiation treatments.

This thesis modernized the capabilities of EPID tumor tracking to account for the complex VMAT treatment now being delivered.   In addition, it showed a possible future direction for future EPID construction by exploring the benefits of a multilayer architecture.   By using imaging parts that are currently available in a different configuration, the cost and complexity of construction are minimized while affording a substantial benefit over the current generation of EPIDs. Beam's-eye-view applications have been relatively neglected due to the poor performance of current flat panel imagers, but that can change with better equipment.   Our work shows that multilayer architecture is a promising avenue for equipment development, with demonstrated improvements measured all the way to clinical utilization.   In addition, future work can look at combining layers with different compositions, so as better to leverage the strengths of different scintillator materials.

List of publications

Peer reviewed journals

A * next to the citation indicates it is used in the thesis publications chapter.

Shi M, *et. al.* A novel method for fast image simulation of flat panel detectors. Phys Med Biol. 2019 Apr 29;64(9):095019. doi: 10.1088/1361-6560/ab12aa.

Myronakis M, *et. al.* Low-dose megavoltage cone-beam computed tomography using a novel multi-layer imager (MLI). Med Phys. 2020 Apr;47(4):1827-1835. doi: 10.1002/mp.14017.

* Ferguson D, **Harris T**, *et. al.* Automated MV markerless tumor tracking for VMAT. Phys Med Biol. 2020 Jun 22;65(12):125011. doi: 10.1088/1361-6560/ab8cd3.

Shi M, *et. al*. A rapid, accurate image simulation strategy for mega-voltage cone-beam computed tomography. Phys Med Biol. 2020 Jul 6;65(13):135004.

Shi M, *et. al*. GPU-accelerated Monte Carlo simulation of MV-CBCT. Phys Med Biol. 2020 Dec 2;65(23):235042.

* **Harris TC**, Seco J, *et. al.* Clinical translation of a new flat-panel detector for beam's-eye-view imaging. Phys Med Biol. 2020 Dec 7;65(22):225004. doi: 10.1088/1361-6560/abb571.

Valencia Lozano I, *et. al.* Frequency-dependent optimal weighting approach for megavoltage multilayer imagers. Phys Med Biol. 2021 Apr 16;66(8). doi: 10.1088/1361-6560/abe051.

Jacobson MW, *et. al.* Abbreviated on-treatment CBCT using roughness penalized mono-energization of kV-MV data and a multi-layer MV imager. Phys Med Biol. 2021 Jun 21;66(13). doi: 10.1088/1361-6560/abddd2.

* **Harris TC**, Seco J, *et. al.* Improvements in beam's eye view fiducial tracking

using a novel multilayer imager. Phys Med Biol. 2021 Jul 7. doi: 10.1088/1361-6560/ac1246.

Conference proceedings

First author posters/talks only.

Harris TC, Seco J, *et. al.* Poster: Convenient Characterization of Megavoltage Flat Panel Modulation Transfer Function by Measuring the Edge Spread Function with a Thin Tantalum Foil. *61st Annual AAPM Meeting*, July 2019.

Harris TC, Seco J, *et. al.* Talk: Clinical Translation of a Novel Megavoltage Multi-Layer Imaging EPID. *62nd Annual AAPM Meeting*, July 2020.

Harris TC, Seco J, *et. al.* Talk: Improvements in Beam's Eye View Fiducial Tracking Using A Novel Multilayer Imager. *63rd Annual AAPM Meeting*, July 2021.

Harris TC, Seco J, *et. al.* Talk: Beam's-Eye-View Imaging of Liver SBRT with a Novel Multi-Layer Imager. *ASTRO Annual Meeting*, October 2021.

Bibliography

Antonuk LE. Electronic portal imaging devices: a review and historical perspective of contemporary technologies and research. Phys Med Biol. 2002 Mar 21;47(6):R31-65.

Atkins KM, Chen Y, Elliott DA, Doshi TS, Ognjenovic S, Vachhani AS, Kishore M, Primack SL, Fuss M, Deffebach ME, Kubicky CD, Tanyi JA. The impact of anatomic tumor location on inter-fraction tumor motion during lung stereotactic body radiation therapy (SBRT). J Radiosurg SBRT. 2015;3(3):203-213.

Fujita H, Tsai DY, Itoh T, Doi K, Morishita J, Ueda K, Ohtsuka A. A simple method for determining the modulation transfer function in digital radiography. IEEE Trans Med Imaging. 1992;11(1):34-9.

Herman MG, Balter JM, Jaffray DA, McGee KP, Munro P, Shalev S, Van Herk M, Wong JW. Clinical use of electronic portal imaging: report of AAPM Radiation Therapy Committee Task Group 58. Med Phys. 2001 May;28(5):712-37.

Hu YH, Myronakis M, Rottmann J, Wang A, Morf D, Shedlock D, Baturin P, Star-Lack J, Berbeco R. A novel method for quantification of beam's-eye-view tumor tracking performance. Med Phys. 2017 Nov;44(11):5650-5659.

Hu YH, Shedlock D, Wang A, Rottmann J, Baturin P, Myronakis M, Huber P, Fueglistaller R, Shi M, Morf D, Star-Lack J, Berbeco RI. Characterizing a novel scintillating glass for application to megavoltage cone-beam computed tomography. Med Phys. 2019 Mar;46(3):1323-1330.

International Electrotechnical Commission 2003 Medical electrical equipment—characteristics of digital x-ray imaging devices—part 1: determination of the detective quantum efficiency, IEC-62220-1

Jaffray DA, Siewerdsen JH, Wong JW, Martinez AA. Flat-panel cone-beam computed tomography for image-guided radiation therapy. Int J Radiat Oncol Biol Phys. 2002 Aug 1;53(5):1337-49.

Kitamura K, Shirato H, Shinohara N, Harabayashi T, Onimaru R, Fujita K, Shimizu S, Nonomura K, Koyanagi T, Miyasaka K. Reduction in acute morbidity using hypofractionated intensity-modulated radiation therapy assisted with a fluoroscopic real-time tumor-tracking system for prostate cancer: preliminary results of a phase I/II study. Cancer J. 2003 Jul-Aug;9(4):268-76.

Kriminski SA, Lovelock DM, Seshan VE, Ali I, Munro P, Amols HI, Fuks Z, Bilsky M, Yamada Y. Comparison of kilovoltage cone-beam computed tomography with megavoltage projection pairs for paraspinal radiosurgery patient alignment and position verification. Int J Radiat Oncol Biol Phys. 2008 Aug 1;71(5):1572-80.

Murphy MJ. Fiducial-based targeting accuracy for external-beam radiotherapy. Med Phys. 2002 Mar;29(3):334-44.

Otto K. Volumetric modulated arc therapy: IMRT in a single gantry arc. Med Phys. 2008 Jan;35(1):310-7.

Shimizu S, Shirato H, Ogura S, Akita-Dosaka H, Kitamura K, Nishioka T, Kagei K, Nishimura M, Miyasaka K. Detection of lung tumor movement in real-time tumor-tracking radiotherapy. Int J Radiat Oncol Biol Phys. 2001 Oct 1;51(2):304-10.

Shirato H, Harada T, Harabayashi T, Hida K, Endo H, Kitamura K, Onimaru R, Yamazaki K, Kurauchi N, Shimizu T, Shinohara N, Matsushita M, Dosaka-Akita H, Miyasaka K. Feasibility of insertion/implantation of 2.0-mm-diameter gold internal fiducial markers for precise setup and real-time tumor tracking in radiotherapy. Int J Radiat Oncol Biol Phys. 2003 May 1;56(1):240-7.

Soete G, De Cock M, Verellen D, Michielsen D, Keuppens F, Storme G. X-ray-assisted positioning of patients treated by conformal arc radiotherapy for prostate cancer: comparison of setup accuracy using implanted markers versus bony structures. Int J Radiat Oncol Biol Phys. 2007 Mar 1;67(3):823-7.

Star-Lack J, Shedlock D, Swahn D, Humber D, Wang A, Hirsh H, Zentai G,

Sawkey D, Kruger I, Sun M, Abel E, Virshup G, Shin M, Fahrig R. A piecewise-focused high DQE detector for MV imaging. Med Phys. 2015 Sep;42(9):5084-99.

Valencia Lozano I, Shi M, Myronakis M, Baturin P, Fueglistaller R, Huber P, Lehmann M, Morf D, Ferguson D, Jacobson MW, Harris T, Berbeco RI, Williams CL. Frequency-dependent optimal weighting approach for megavoltage multilayer imagers. Phys Med Biol. 2021 Apr 16;66(8).

Xu Q, Hanna G, Grimm J, Kubicek G, Pahlajani N, Asbell S, Fan J, Chen Y, LaCouture T. Quantifying rigid and nonrigid motion of liver tumors during stereotactic body radiation therapy. Int J Radiat Oncol Biol Phys. 2014 Sep 1;90(1):94-101.

Acknowledgements

I would like to thank everyone who made this thesis possible. In particular I would like to thank Prof. Dr. Joao Seco and Prof. Dr. Ross Berbeco for their advice and guidance throughout the research. They have been excellent supervisors, and I owe them for any strides I have made the past few years. This work would have been impossible without them.

I would like to thank Prof. Dr. Jürgen Hesser for agreeing to act as referee for this thesis. Additional gratitude to Prof. Dr. Cornelis Dullemond and Prof. Dr. Norbert Herrmann for becoming committee members for the examination.

I give my sincere appreciation to my Dana-Farber/Brigham and Women's Cancer Center collaborators. Dr. Dianne Ferguson, Prof. Dr. Matt Jacobson, Dr. Marios Myronakis, Dr. Mengying Shi, Dr. Ingrid Valenica, Lozano, and Prof. Dr. Yue-Houng Hu in particular gave important feedback and advice along the way. Our Varian collaborators, especially Dr. Mathias Lehmann and Dr. Pascal Huber, were invaluable with their technical expertise.

And finally, my gratitude to my friends and family for their support and patience during my studies. I cannot praise Montie enough for her encouragement and for always being there for me… and learning entirely too much about EPIDs for a psychiatrist along the way.